PHYSICAL REVIEW B **71**, 045120 (2005)

Electronic Raman scattering in correlated materials: A treatment of nonresonant, mixed, and resonant scattering using dynamical mean-field theory

A. M. Shvaika* and O. Vorobyov†
Institute for Condensed Matter Physics of the National Academy of Sciences of Ukraine, 1 Svientsitskii Street, 79011 Lviv, Ukraine

J. K. Freericks‡
Department of Physics, Georgetown University, Washington, DC 20057, USA

T. P. Devereaux§
Department of Physics, University of Waterloo, Ontario, Canada N2L 3GI

(Received 18 August 2004; revised manuscript received 21 October 2004; published 25 January 2005)

We solve for the electronic Raman scattering response functions on an infinite-dimensional hypercubic lattice employing dynamical mean-field theory. This contribution extends previous work on the nonresonant response to include the mixed and resonant contributions. We focus our attention on the infinite-dimensional spinless Falicov-Kimball model, where the problem can be solved exactly, and the system can be tuned to go through a Mott-Hubbard-like metal-insulator transition. Resonant effects vary in different scattering geometries, corresponding to the symmetries of the charge excitations scattered by the light. We do find that the Raman response is large near the double resonance, where the transfered frequency is close to the incident photon frequency. We also find a joint resonance of both the charge-transfer peak and the low-energy peak when the incident photon frequency is on the order of the interaction strength. In general, the resonance effects can create order of magnitude (or more) enhancements of features in the nonresonant response, especially when the incident photon frequency is somewhat larger than the frequency of the nonresonant feature. Finally, we find that the resonant effects also exhibit isosbestic behavior, even in the A_{1g} and B_{2g} sectors, and it is most prominent when the incident photon frequency is on the order of the interaction energy.

DOI: 10.1103/PhysRevB.71.045120 PACS number(s): 78.30.−j, 71.10.−w, 71.27.+a, 71.30.+h

I. INTRODUCTION

Electronic Raman scattering has long been used as a direct probe of electronic charge excitations. Experiments have shown a number of interesting phenomena, especially in correlated materials. A material independence for Raman scattering has been seen in a number of different correlation gap (insulating) materials ranging from FeSi,[1] to SmB_6,[2] to $Ca_3Ru_2O_7$,[3] to high temperature superconductors.[4–6] The Raman response shows a gap opening at low temperature, but with the gap about ten times larger than the onset temperature where the gap starts to form. In addition, an isosbestic point is often seen, where the Raman response at one value of frequency is independent of temperature (at low temperature), and curves for different temperatures appear to cross at a single point. Resonant effects are even more interesting, as it is believed that the resonance can cause an enhancement of the nonresonant signal by orders of magnitude, and allow small signals to become observable. What remains unknown is whether these resonant enhancements dramatically change the shape of the underlying nonresonant response.

The theoretical description of electronic Raman scattering has lagged behind experiment. Recently, dynamical mean field theory (DMFT) has been employed to calculate the nonresonant response in the Falicov-Kimball[7] and Hubbard models[8] and to examine inelastic x-ray scattering as well.[9] It was found that the theoretical calculations of the nonresonant response show much of the behavior seen in experiment, including the large gap relative to the onset temperature and the generic appearance of an easily observed isosbestic point in the B_{1g} channel.

However, it is well known that many of the Raman signals in correlated metals and insulators display complicated dependences on the incoming photon frequency ω_i. The resonant behavior of the B_{1g} two-magnon feature at roughly 340 meV has been well studied in the parent insulating cuprates La_2CuO_4, $YBa_2Cu_3O_6$, and $Sr_2CuO_2Cl_2$,[4] where a resonance is found for incident photon energies near 3 eV. Although recent progress has been made,[10,11] the reason for this resonance is not clear since the resonance frequency lies above the optical absorption edge frequency measured in the dielectric response,[5] and the photon energy is much larger than the location of the resonance peak in the response function.

The general question of how the low-energy features (such as particle-hole excitations near the Fermi level) and high-energy (such as charge-transfer excitations) change under resonant conditions remains relatively unexplored. Most treatments for Raman scattering in insulators have focused on only the spin degrees of freedom (Heisenberg limit) in two dimensions. For the case when the incident photon energy is much less than the optical band gap, the Loudon-Fleury theory[12] has been widely employed to determine resonance profiles from spin degrees of freedom via series expansions,[13] exact diagonalization of small clusters[14] or quantum Monte Carlo simulations[15] of the Heisenberg model. Modifications due to quantum fluctuations,[13,15] bilayers,[16] four-magnon processes,[17] couplings beyond nearest neighbor exchange,[18] and ring exchange[19] have all been taken into account to give a thorough treatment of two magnon scattering from spin degrees of freedom in the nonresonant regime. These approaches fail when the laser frequency is tuned to lie near an optical transition. In this regime, based on a spin-density-wave approach, Frenkel, Chubukov, and Morr have formulated a so-called "triple-resonance" theory from which important features of the spectra can be derived.[10] While good agreement was obtained for the resonant profile of the two magnon contribution to light scattering,[5] general features not related to the two-magnon peak are missed and lineshape calculations are complex and only semiquantitative.

An approach treating the full fermionic degrees of freedom is still lacking. Recently exact diagonalization studies of the Hubbard model have been employed to yield line shapes in the resonant limit from both spin and charge degrees of freedom.[11] Yet the nonresonant and mixed terms were not taken into account. These calculations also suffer the problems related to the finite size of the clusters (such as artificially broadening the delta functions to approximate thermodynamic-limit spectra). So generally, there is no theory for Raman scattering from both charge and spin degrees of freedom which predicts spectral line shapes where all resonant, mixed, and nonresonant terms are treated on an equal footing and do not suffer from finite-size effects.

In this contribution we illustrate how to calculate the full electronic Raman response function, including contributions from the nonresonant, mixed, and resonant processes within a single-band model. Our model includes interactions of the photon with all charge excitations of a correlated fermionic system, but does not take into account any scattering off of spin excitations. The scattering response is a complicated function of the correlations, the temperature, the incident photon energy, and the transfered energy. A short communication of this work has already appeared.[20]

Little is known about what the mixed Raman response looks like. We find that, as opposed to the nonresonant and resonant responses, which are manifestly positive, the mixed response is often negative (although the total response always remains positive). The resonant response is expected to be large in the region where the transfered energy approaches the incident photon energy, called the double resonance, because the energy denominators of two pairs of the Green's functions in the bare response function approach zero. Interesting results are also anticipated in the strongly coupled (Mott-insulating) regime, when the incident photon energy is close to the interaction energy. Indeed, we find this is the case here. We also examine the situation where the initial photon energy is larger than the excitation energies in the correlated band. This is the most common experimental situation in correlated materials with renormalized low-energy "bands." The mixed and resonant responses also behave differently than the nonresonant response when we compare the Stokes (energy transfered from the photon to the electrons) and the anti-Stokes (energy transfered from the electrons to the photons) responses. These are equal for nonresonant scattering, but the anti-Stokes response is much smaller than the Stokes response for the mixed and resonant scattering cases (introducing an asymmetry to the Raman scattering).

The theoretical challenge in calculating the full inelastic light scattering response function is that the mixed diagrams involve three-particle susceptibilities and the resonant diagrams involve four-particle susceptibilities. It is only in the infinite-dimensional limit, where most of the many-particle vertex renormalizations vanish (all three-particle and four-particle vertices do not contribute; only the two-particle vertices enter), can one imagine performing the calculation of these susceptibilities exactly. Note that it is well known that the irreducible two-particle vertices contain nonlocal terms in infinite dimensions.[21] Which terms from the irreducible vertex, local or nonlocal, contribute to the final response depends on the symmetry, scaling and momentum dependence of the external vertices. As a result, in many cases (in particular for optical light scattering where we approximate the photon momenta by $\boldsymbol{k}_i=\boldsymbol{k}_f=0$) we find that the momentum dependence is so weak, that whenever a momentum argument of the vertex function is summed over the Brillouin zone, it can be replaced by the local vertex.[22,23] The situation is more complex for the three- or four-particle vertices, but a strong-coupling pertubation theory shows that the momentum dependence continues to be weak (to lowest order), so we use the local vertices in all response functions. It turns out that because the two-particle irreducible charge vertex is known exactly for the Falicov-Kimball model,[24] one can calculate the full Raman response function in this case (since the general form of the charge vertex is not known for the Hubbard model, one can only perform approximate calculations for that system even in infinite dimensions; nevertheless, the diagrammatic analysis given in Sec. III holds for the Hubbard model, we just are not able to evaluate the final expressions).

We evaluate our exact expressions numerically and study their evolution as functions of the incident light energy and of the transfered energy. In the case of a correlated metal, we show how Fermi-liquid-like features evolve as the lifetime of putative quasiparticles decreases due to scattering. The results are even more interesting in the correlated insulator. We examine what happens to the isosbestic point identified in the nonresonant response, and how the presence of the charge gap affects the optical scattering.

Inelastic light scattering involves a coupling of photons to electronic charge excitations of the correlated material. The symmetry of the incident and scattered light relates to the symmetry of the charge excitations that are coupled to the light. There are typically three symmetries examined in experiments. The A_{1g} symmetry has the full symmetry of the lattice. This is measured, in a system with only nearest-neighbor hopping, by polarizing the incident and scattered light along the diagonal direction of the hypercubic lattice, so in large dimensions, we take the initial and final polarizations to be $e^i=e^f=(1,1,1,\ldots)$. The B_{1g} symmetry is a d-wave-like symmetry that involves crossed polarizers along the diagonals. We take $e^i=(1,1,1,\ldots)$ and $e^f=(-1,1,-1,1,\ldots)$ for the B_{1g} channel. Finally, the B_{2g} symmetry is another d-wave symmetry rotated by 45 degrees; it requires the polarizations to satisfy $e^i=(1,0,1,0,\ldots)$ and $e^f=(0,1,0,1,\ldots)$. It turns out that the A_{1g} sector has contributions from nonresonant, mixed, and resonant Raman scattering, the B_{1g} sector has contributions from nonresonant and resonant Raman scattering only, and the B_{2g} sector is purely resonant. This is generally true for a model on a bipartite lattice with nearest-neighbor hopping only. If longer-range hoppings are allowed, then all channels will have nonresonant, mixed and resonant contributions.

While our approach towards analytic continuation is general, the overall complexity of the problem limits our evaluation of the light scattering cross section. By focusing on the spinless Falicov-Kimball model, we present a theory of light scattering from charge degrees of freedom only; valid for any incoming photon frequency. However, we are not able to address scattering from spin degrees of freedom resulting in two-magnon Raman scattering, for example. Nevertheless, we expect that our results help frame the physics related to resonance phenomena in paramagnetic correlated metals and insulators, and the behavior near a metal-insulator transition.

Our plan of the paper is as follows. In Sec. II, we describe the general analytic-continuation formula that carries one from a time-ordered correlation function on the imaginary axis to the real response function. The formulas are completely general, and hold for the case of inelastic scattering of x-rays as well. The challenge is in evaluating the corresponding response functions along the real axis, which we know how to do only for the Falicov-Kimball model in infinite dimensions. In Sec. III, we evaluate the Raman scattering for the Falicov-Kimball model explicitly, calculating all response functions, and showing in detail how to perform all of the relevant renormalizations of the two-, three-, and four-particle correlation functions. In Sec. IV, we present our numerical results for Raman scattering at half filling. We examine the metallic case, the insulating case, and study the evolution of the Raman response as a function of the incident photon energy. We present our conclusions in Sec. V.

II. GENERAL ANALYTIC CONTINUATION FORMALISM

Our starting point is the expression for the inelastic light scattering cross section derived by Shastry and Shraiman[25]

$$R(\boldsymbol{q},\Omega) = 2\pi \sum_{i,f} \exp(-\beta\varepsilon_i)\,\delta(\varepsilon_f - \varepsilon_i - \Omega) \times \left| g(\boldsymbol{k}_i) g(\boldsymbol{k}_f) e^i_\alpha e^f_\beta \left\langle f \middle| \hat{M}^{\alpha\beta}(\boldsymbol{q}) \middle| i \right\rangle \right|^2 / \mathcal{Z} \tag{2.1}$$

for the scattering of electrons by photons of arbitrary wavelength (the repeated indices α and β are summed over). Here $\Omega = \omega_i - \omega_f$ and $\boldsymbol{q} = \boldsymbol{k}_i - \boldsymbol{k}_f$ are the transfered energy and momentum, respectively, while $\omega_{i(f)}$, $\boldsymbol{k}_{i(f)}$, and $\boldsymbol{e}^{i(f)}$ denote the energy, momentum and polarization of the initial (final) states of the photons, $\varepsilon_{i(f)}$ refer to the eigenstates describing the "electronic matter," and $g(\boldsymbol{q}) = (hc^2/V\omega_{\boldsymbol{q}})^{1/2}$ is the "scattering strength" with $\omega_{\boldsymbol{q}} = c|\boldsymbol{q}|$. Lastly, $\mathcal{Z}$ is the partition function. For an electronic system with nearest-neighbor hopping, the interaction with a weak external transverse electromagnetic field $\boldsymbol{A}$ is described by the following interacting Hamiltonian

$$H_{\text{int}} = -\frac{e}{\hbar c} \sum_{\boldsymbol{k}} \boldsymbol{j}(\boldsymbol{k}) \cdot \boldsymbol{A}(-\boldsymbol{k}) + \frac{e^2}{2\hbar^2 c^2} \sum_{\boldsymbol{k}\boldsymbol{k}'} A_\alpha(-\boldsymbol{k})\,\gamma_{\alpha,\beta}(\boldsymbol{k}+\boldsymbol{k}') A_\beta(-\boldsymbol{k}'), \tag{2.2}$$

where

$$j_\alpha(\boldsymbol{q}) = \sum_{\boldsymbol{k}} v_\alpha(\boldsymbol{k}) c^\dagger_\sigma(\boldsymbol{k}+\boldsymbol{q}/2) c_\sigma(\boldsymbol{k}-\boldsymbol{q}/2),$$

$$v_\alpha(\boldsymbol{k}) = \frac{\partial\varepsilon(\boldsymbol{k})}{\partial k_\alpha} \tag{2.3}$$

are the current operator and Fermi velocity, respectively, and

$$\gamma_{\alpha,\beta}(\boldsymbol{q}) = \sum_{\boldsymbol{k}} \frac{\partial^2\varepsilon(\boldsymbol{k})}{\partial k_\alpha \partial k_\beta} c^\dagger_\sigma(\boldsymbol{k}+\boldsymbol{q}/2) c_\sigma(\boldsymbol{k}-\boldsymbol{q}/2) \tag{2.4}$$

is the so-called stress tensor. As a result, the scattering operator $\hat{M}(\boldsymbol{q})$ has both nonresonant and resonant contributions

$$\langle f | M^{\alpha\beta}(\boldsymbol{q}) | i \rangle = \langle f | \gamma_{\alpha,\beta}(\boldsymbol{q}) | i \rangle + \sum_l \left(\frac{\langle f | j_\beta(\boldsymbol{k}_f) | l \rangle \langle l | j_\alpha(-\boldsymbol{k}_i) | i \rangle}{\varepsilon_l - \varepsilon_i - \omega_i} + \frac{\langle f | j_\alpha(-\boldsymbol{k}_i) | l \rangle \langle l | j_\beta(\boldsymbol{k}_f) | i \rangle}{\varepsilon_l - \varepsilon_i + \omega_f} \right), \tag{2.5}$$

with the sum l over intermediate states. The term with the stress tensor is the nonresonant contribution, while the term with the square of the current operator is the resonant contribution. Now the Raman-scattering cross section contains nonresonant, mixed, and resonant contributions (because it is constructed from the square of the scattering operator):

$$R(\boldsymbol{q},\Omega) = R_N(\boldsymbol{q},\Omega) + R_M(\boldsymbol{q},\Omega) + R_R(\boldsymbol{q},\Omega), \tag{2.6}$$

where the nonresonant contribution is

$$R_N(\boldsymbol{q},\Omega) = 2\pi g^2(\boldsymbol{k}_i) g^2(\boldsymbol{k}_f) \times \sum_{i,f} \frac{\exp(-\beta\varepsilon_i)}{\mathcal{Z}} \tilde{\gamma}_{i,f} \tilde{\gamma}_{f,i}\, \delta(\varepsilon_f - \varepsilon_i - \Omega), \tag{2.7}$$

the mixed contribution is

$$R_M(\boldsymbol{q},\Omega) = 2\pi g^2(\boldsymbol{k}_i) g^2(\boldsymbol{k}_f) \sum_{i,f,l} \frac{\exp(-\beta\varepsilon_i)}{\mathcal{Z}} \times \left[\tilde{\gamma}_{i,f} \left(\frac{j^{(f)}_{f,l} j^{(i)}_{l,i}}{\varepsilon_l - \varepsilon_i - \omega_i + i0^+} + \frac{j^{(i)}_{f,l} j^{(f)}_{l,i}}{\varepsilon_l - \varepsilon_i + \omega_f - i0^+} \right) + \left(\frac{j^{(i)}_{i,l} j^{(f)}_{l,f}}{\varepsilon_l - \varepsilon_i - \omega_i - i0^+} + \frac{j^{(f)}_{i,l} j^{(i)}_{l,f}}{\varepsilon_l - \varepsilon_i + \omega_f + i0^+} \right) \tilde{\gamma}_{f,i} \right] \times \delta(\varepsilon_f - \varepsilon_i - \Omega), \tag{2.8}$$

and the resonant contribution is

$$R_R(\boldsymbol{q},\Omega) = 2\pi g^2(\boldsymbol{k}_i) g^2(\boldsymbol{k}_f) \sum_{i,f,l,l'} \frac{\exp(-\beta\varepsilon_i)}{\mathcal{Z}} \times \left(\frac{j^{(i)}_{i,l} j^{(f)}_{l,f}}{\varepsilon_l - \varepsilon_i - \omega_i - i0^+} + \frac{j^{(f)}_{i,l} j^{(i)}_{l,f}}{\varepsilon_l - \varepsilon_i + \omega_f + i0^+} \right) \times \left(\frac{j^{(f)}_{f,l'} j^{(i)}_{l',i}}{\varepsilon_{l'} - \varepsilon_i - \omega_i + i0^+} + \frac{j^{(i)}_{f,l'} j^{(f)}_{l',i}}{\varepsilon_{l'} - \varepsilon_i + \omega_f - i0^+} \right) \times \delta(\varepsilon_f - \varepsilon_i - \Omega). \tag{2.9}$$

In these equations, we have introduced the following symbols

$$\tilde{\gamma} = \sum_{\alpha\beta} e^{i}_{\alpha}\gamma_{\alpha,\beta}(\boldsymbol{q})e^{f}_{\beta},$$

$$j^{(i)} = \sum_{\alpha} e^{i}_{\alpha} j_{\alpha}(-\boldsymbol{k}_i),$$

$$j^{(f)} = \sum_{\alpha} e^{f}_{\alpha} j_{\alpha}(\boldsymbol{k}_f), \tag{2.10}$$

with the notation $A_{i,f} = \langle i|A|f\rangle$ for the matrix elements of an operator A.

We evaluate these expressions by a Green's function technique that starts from correlation functions evaluated on the imaginary axis and then performs an analytic continuation to the real axis to get the physical response functions. Our strategy is to first consider the analytic continuation procedure in a general sense, which holds for any model Hamiltonian and for arbitrary momentum transfer. We will derive connection formulas between the Matsubara frequency axis correlation functions and the analytically continued response functions on the real axis. But those expressions will require us to be able to evaluate a number of different susceptibilities, and those expressions are not known for arbitrary Hamiltonians. We will show how to evaluate them exactly for the infinite-dimensional Falicov-Kimball model in the next section.

A. Nonresonant scattering

The nonresonant scattering in Eq. (2.7) is proportional to the spectral density function. The spectral density cannot be calculated directly but is instead obtained from the analytic continuation of the imaginary-time response function constructed from the time-ordered product of two stress-tensor operators

$$\chi^{(2)}_{\tilde{\gamma},\tilde{\gamma}}(\tau,\tau') = \langle \mathcal{T}_{\tau}\tilde{\gamma}(\tau)\tilde{\gamma}(\tau')\rangle \tag{2.11}$$

with the τ dependence of the operator determined by the Hamiltonian in the absence of the electromagnetic field (the symbol $\mathcal{T}_{\tau}$ denotes time ordering). The first step is to calculate the double Fourier transformation to the Matsubara frequency axis

$$\chi^{(2)}_{\tilde{\gamma},\tilde{\gamma}}(i\nu_l,i\nu_n) = T\int_0^{\beta} d\tau\int_0^{\beta} d\tau'\, e^{i\nu_l\tau}\chi^{(2)}_{\tilde{\gamma},\tilde{\gamma}}(\tau,\tau')e^{i\nu_n\tau'} \tag{2.12}$$

for bosonic Matsubara frequencies $i\nu_n = i\pi T2n$ with $\beta = 1/T$. In thermal equilibrium, the two-particle correlation function depends only on the difference of the two time variables, so the double Fourier transform becomes a "diagonal" function, evaluated as

$$\chi^{(2)}_{\tilde{\gamma},\tilde{\gamma}}(-i\nu,i\nu) = \sum_{i,f}\frac{\exp(-\beta\varepsilon_i)}{\mathcal{Z}}\frac{\tilde{\gamma}_{i,f}\tilde{\gamma}_{f,i}}{\varepsilon_f-\varepsilon_i-i\nu} \times[1-\exp(\beta(\varepsilon_i-\varepsilon_f))]. \tag{2.13}$$

In order to extract the spectral density of states from the Matsubara correlation function in Eq. (2.13), we perform the analytic continuation $i\nu \rightarrow \Omega \pm i0^{+}$ which yields for the nonresonant scattering the known expression

$$R_N(\boldsymbol{q},\Omega) = \frac{2\pi g^2(\boldsymbol{k}_i)g^2(\boldsymbol{k}_f)}{1-\exp(-\beta\Omega)}\chi_N(\boldsymbol{q},\Omega), \tag{2.14}$$

where we introduced the nonresonant response function

$$\chi_N(\boldsymbol{q},\Omega) = \frac{1}{2\pi i}\{\chi^{(2)}_{\tilde{\gamma},\tilde{\gamma}}(-\Omega-i0^{+},\Omega+i0^{+}) - \chi^{(2)}_{\tilde{\gamma},\tilde{\gamma}}(-\Omega+i0^{+},\Omega-i0^{+})\} \tag{2.15}$$

evaluated on the real axis. A similar strategy is used to determine the mixed and resonant contributions as described in the next two subsections.

B. Mixed scattering

In the case of mixed scattering in Eq. (2.8), the calculation begins with the multitime correlation function constructed from the stress tensor and two current operators

$$\chi^{(3)}_{\tilde{\gamma},f,i}(\tau,\tau',\tau'') = \langle \mathcal{T}_{\tau}\tilde{\gamma}(\tau)j^{(f)}(\tau')j^{(i)}(\tau'')\rangle. \tag{2.16}$$

We define the Fourier transform as before, with respect to three Matsubara frequencies (all with the same sign of the exponent). Once again, in thermal equilibrium we have imaginary-time-translation invariance, so the sum of the three Matsubara frequencies must vanish, yielding

$$\begin{aligned}
\chi^{(3)}_{\tilde{\gamma},f,i}&(i\nu_1,i\nu_2,i\nu_3)\\
&= \delta(\nu_1+\nu_2+\nu_3)\frac{1}{\mathcal{Z}}\Bigg\{\sum_{i,f,l}\tilde{\gamma}_{i,f}j^{(f)}_{f,l}j^{(i)}_{l,i}\\
&\times\Bigg[\frac{\exp(-\beta\varepsilon_i)}{(\varepsilon_f-\varepsilon_i+i\nu_1)(\varepsilon_l-\varepsilon_i-i\nu_3)}\\
&+\frac{\exp(-\beta\varepsilon_f)}{(\varepsilon_l-\varepsilon_f+i\nu_2)(\varepsilon_i-\varepsilon_f-i\nu_1)}\\
&+\frac{\exp(-\beta\varepsilon_l)}{(\varepsilon_i-\varepsilon_l+i\nu_3)(\varepsilon_f-\varepsilon_l-i\nu_2)}\Bigg]\\
&+\sum_{i,f,l}j^{(i)}_{i,l}j^{(f)}_{l,f}\tilde{\gamma}_{f,i}\Bigg[\frac{\exp(-\beta\varepsilon_i)}{(\varepsilon_f-\varepsilon_i-i\nu_1)(\varepsilon_l-\varepsilon_i+i\nu_3)}\\
&+\frac{\exp(-\beta\varepsilon_f)}{(\varepsilon_l-\varepsilon_f-i\nu_2)(\varepsilon_i-\varepsilon_f+i\nu_1)}\\
&+\frac{\exp(-\beta\varepsilon_l)}{(\varepsilon_i-\varepsilon_l-i\nu_3)(\varepsilon_f-\varepsilon_l+i\nu_2)}\Bigg]\Bigg\}
\end{aligned} \tag{2.17}$$

which contains $3!=6$ terms collected into two groups of terms connected by cyclic permutations $\mathcal{P}$, with

$$\chi^{(3)}_{A,B,C}(i\nu_1,i\nu_2,i\nu_3) = \chi^{(3)}_{A^{\dagger},B^{\dagger},C^{\dagger}}(-i\nu_1,-i\nu_2,-i\nu_3). \tag{2.18}$$

After analytic continuation $i\nu_{\alpha} \rightarrow z_{\alpha}$ with the constraint

$$z_1 + z_2 + z_3 = 0, \tag{2.19}$$

one can see that the expression in Eq. (2.17) has three branch cuts when $\mathrm{Im}\, z_\alpha \to 0^\pm$ (for $\alpha=1$, 2, or 3). Note that the constraint in Eq. (2.19) forbids only two of the z_α's to simultaneously have $\mathrm{Im}\, z_\alpha = 0^\pm$, but the imaginary part of all three can vanish simultaneously. In order to produce the expression for the mixed Raman cross section in Eq. (2.8), we need to focus on the branch cuts that occur when $z_1 \to -\Omega \pm i0^+$ and $z_1 \to \Omega \pm i0^+$ in order to produce the appropriate δ-function and matrix elements in the mixed scattering cross section. The corresponding discontinuity across the branch cut when $\mathrm{Im}\, z_1 = 0$, occurs when the terms in Eq. (2.17) are analytically continued with z_1 moving onto the real axis. In the first case when $z_1 \to -\Omega \pm i0^+$, and $z_2 \to \Omega - z_3$, we find

$$\begin{aligned}
&\frac{1}{2\pi i}\chi^{(3)}_{\tilde{\gamma},f,i}(z_1,z_2,z_3)\Bigg|^{z_1\to-\Omega-i0^+}_{z_1\to-\Omega+i0^+} \\
&= \frac{1}{2\pi i}[\chi^{(3)}_{\tilde{\gamma},f,i}(-\Omega - i0^+, \Omega - z_3, z_3) \\
&\quad - \chi^{(3)}_{\tilde{\gamma},f,i}(-\Omega + i0^+, \Omega - z_3, z_3)] \\
&= (1 - e^{-\beta\Omega})\sum_{i,f,l}\frac{e^{-\beta\varepsilon_i}}{\mathcal{Z}}\tilde{\gamma}_{i,f}\left[\frac{j^{(f)}_{f,l}j^{(i)}_{l,i}}{\varepsilon_l - \varepsilon_i - z_3} + \frac{j^{(i)}_{f,l}j^{(f)}_{l,i}}{\varepsilon_l - \varepsilon_f + z_3}\right] \\
&\quad \times \delta(\varepsilon_f - \varepsilon_i - \Omega).
\end{aligned} \tag{2.20}$$

The sum on the right-hand side of Eq. (2.20), with $z_3 = \omega_i - i0^+$, is proportional to the first two terms in Eq. (2.8). In a similar way we can derive last two terms in Eq. (2.8) from the branch cut $z_1 \to \Omega \pm i0^+$, and $z_2 \to -\Omega - z_3$ (one also interchanges $i \leftrightarrow f$). Hence, we arrive at the general expression for the mixed scattering

$$R_M(\boldsymbol{q},\Omega) = \frac{2\pi g^2(\boldsymbol{k}_i)g^2(\boldsymbol{k}_f)}{1 - \exp(-\beta\Omega)}\chi_M(\boldsymbol{q},\Omega) \tag{2.21}$$

with the mixed Raman response function defined by

$$\begin{aligned}
\chi_M(\boldsymbol{q},\Omega) = \frac{1}{2\pi i}&[\chi^{(3)}_{\tilde{\gamma},f,i}(-\Omega - i0^+, -\omega_f + i0^+, \omega_i - i0^+) \\
&- \chi^{(3)}_{\tilde{\gamma},f,i}(-\Omega + i0^+, -\omega_f + i0^+, \omega_i - i0^+) \\
&+ \chi^{(3)}_{\tilde{\gamma},f,i}(\Omega + i0^+, \omega_f + i0^+, -\omega_i - i0^+) \\
&- \chi^{(3)}_{\tilde{\gamma},f,i}(\Omega - i0^+, \omega_f + i0^+, -\omega_i - i0^+)]
\end{aligned} \tag{2.22}$$

on the real axis. The operators $\tilde{\gamma}(\boldsymbol{q})$, $j^{(f)}(\boldsymbol{k}_f)$ and $j^{(i)}(\boldsymbol{k}_i)$ are Hermitian for optical light scattering, which has vanishing momentum $\boldsymbol{k}_i = \boldsymbol{k}_f = \boldsymbol{q} = 0$, and, with the use of Eq. (2.18), one can change the sign of all of the frequency arguments in the first two terms of Eq. (2.22).

C. Resonant scattering

For the resonant scattering case in Eq. (2.9), the procedure is similar: one has to calculate the multitime correlation function constructed from the four current operators

$$\chi^{(4)}_{i,f,f,i}(\tau_1,\tau_2,\tau_3,\tau_4) = \langle \mathcal{T}_\tau j^{(i)}(\tau_1) j^{(f)}(\tau_2) j^{(f)}(\tau_3) j^{(i)}(\tau_4)\rangle. \tag{2.23}$$

Once again, defining the Fourier transform in terms of four Matsubara frequencies (with the same sign in the exponent) yields the following result (with the delta function arising from the time-translation invariance)

$$\begin{aligned}
\chi^{(4)}_{i,f,f,i}(i\nu_1,i\nu_2,i\nu_3,i\nu_4) = \delta(\nu_1 + \nu_2 + \nu_3 + \nu_4)& \\
\times[\tilde{\chi}^{(4)}_{i,f,f,i}(i\nu_1,i\nu_2,i\nu_3,i\nu_4)& \\
+ \tilde{\chi}^{(4)}_{i,f,i,f}(i\nu_1,i\nu_2,i\nu_4,i\nu_3)& \\
+ \chi^{(4)}_{i,i,f,f}(i\nu_1,i\nu_4,i\nu_2,i\nu_3)]&.
\end{aligned} \tag{2.24}$$

Here we introduce the generic four-particle susceptibility

$$\begin{aligned}
&\tilde{\chi}^{(4)}_{A,B,C,D}(i\nu_1,i\nu_2,i\nu_3,i\nu_4) \\
&\quad = \sum_{i,f,l,l'} A_{i,l}B_{l,f}C_{f,l'}D_{l',i}\frac{1}{\mathcal{Z}} \\
&\quad \times\Bigg[\frac{\exp(-\beta\varepsilon_i)}{(\varepsilon_l - \varepsilon_i + i\nu_1)(\varepsilon_{l'} - \varepsilon_i - i\nu_4)(\varepsilon_f - \varepsilon_i - i\nu_3 - i\nu_4)} \\
&\quad + \frac{\exp(-\beta\varepsilon_l)}{(\varepsilon_f - \varepsilon_l + i\nu_2)(\varepsilon_i - \varepsilon_l - i\nu_1)(\varepsilon_{l'} - \varepsilon_l - i\nu_4 - i\nu_1)} \\
&\quad + \frac{\exp(-\beta\varepsilon_f)}{(\varepsilon_{l'} - \varepsilon_f + i\nu_3)(\varepsilon_l - \varepsilon_f - i\nu_2)(\varepsilon_i - \varepsilon_f - i\nu_1 - i\nu_2)} \\
&\quad + \frac{\exp(-\beta\varepsilon_{l'})}{(\varepsilon_i - \varepsilon_{l'} + i\nu_4)(\varepsilon_f - \varepsilon_{l'} - i\nu_3)(\varepsilon_f - \varepsilon_{l'} - i\nu_2 - i\nu_3)}\Bigg] \\
&\quad + \sum_{i,f,l,l'} D_{i,l'}C_{l',f}B_{f,l}A_{l,i}\frac{1}{\mathcal{Z}} \\
&\quad \times\Bigg[\frac{\exp(-\beta\varepsilon_i)}{(\varepsilon_l - \varepsilon_i - i\nu_1)(\varepsilon_{l'} - \varepsilon_i + i\nu_4)(\varepsilon_f - \varepsilon_i + i\nu_3 + i\nu_4)} \\
&\quad + \frac{\exp(-\beta\varepsilon_l)}{(\varepsilon_f - \varepsilon_l - i\nu_2)(\varepsilon_i - \varepsilon_l + i\nu_1)(\varepsilon_{l'} - \varepsilon_l + i\nu_4 + i\nu_1)} \\
&\quad + \frac{\exp(-\beta\varepsilon_f)}{(\varepsilon_{l'} - \varepsilon_f - i\nu_3)(\varepsilon_l - \varepsilon_f + i\nu_2)(\varepsilon_i - \varepsilon_f + i\nu_1 + i\nu_2)} \\
&\quad + \frac{\exp(-\beta\varepsilon_{l'})}{(\varepsilon_i - \varepsilon_{l'} - i\nu_4)(\varepsilon_f - \varepsilon_{l'} + i\nu_3)(\varepsilon_f - \varepsilon_{l'} + i\nu_2 + i\nu_3)}\Bigg]
\end{aligned} \tag{2.25}$$

with

$$\tilde{\chi}^{(4)}_{A,B,C,D}(i\nu_1,i\nu_2,i\nu_3,i\nu_4) = \tilde{\chi}^{(4)}_{A^\dagger,B^\dagger,C^\dagger,D^\dagger}(-i\nu_1,-i\nu_2,-i\nu_3,-i\nu_4). \tag{2.26}$$

The expression in Eq. (2.24) contains $4! = 24$ terms collected into six different groups of the terms, with each group member connected by the cyclic permutation of four objects.

After analytic continuation $i\nu_\alpha \to z_\alpha$ with the constraint

$$z_1 + z_2 + z_3 + z_4 = 0, \tag{2.27}$$

one can see that the expression in Eq. (2.24) has branch cuts when any Im $z_\alpha \to 0^\pm$ or when any pair Im$(z_\alpha + z_\beta) \to 0^\pm$. The δ-function in the expression for the resonant scattering cross section in Eq. (2.9) is connected to the branch cut at $z_3 + z_4 = -z_1 - z_2 \to \Omega \pm i0^+$ and the discontinuity of the response function across this branch cut is equal to

$$\begin{aligned}
&\frac{1}{2\pi i}\chi^{(4)}_{i,f,f,i}(z_1,z_2,z_3,z_4)\Bigg|^{z_3+z_4=-z_1-z_2\to\Omega+i0^+}_{z_3+z_4=-z_1-z_2\to\Omega-i0^+} \\
&= (1-e^{-\beta\Omega})\sum_{i,f,l,l'}\frac{e^{-\beta\varepsilon_i}}{\mathcal{Z}}\delta(\varepsilon_f-\varepsilon_i-\Omega) \\
&\times\Bigg[\frac{j^{(i)}_{i,l}j^{(f)}_{l,f}j^{(f)}_{f,l'}j^{(i)}_{l'i}}{(\varepsilon_l-\varepsilon_i+z_1)(\varepsilon_{l'}-\varepsilon_i-\Omega+z_3)} \\
&+\frac{j^{(f)}_{i,l}j^{(i)}_{l,f}j^{(i)}_{f,l'}j^{(f)}_{l',i}}{(\varepsilon_l-\varepsilon_i-\Omega-z_1)(\varepsilon_{l'}-\varepsilon_i-z_3)} \\
&+\frac{j^{(i)}_{i,l}j^{(f)}_{l,f}j^{(i)}_{f,l'}j^{(f)}_{l',i}}{(\varepsilon_l-\varepsilon_i+z_1)(\varepsilon_{l'}-\varepsilon_i-z_3)} \\
&+\frac{j^{(f)}_{i,l}j^{(i)}_{l,f}j^{(f)}_{f,l'}j^{(i)}_{l',i}}{(\varepsilon_l-\varepsilon_i-\Omega-z_1)(\varepsilon_{l'}-\varepsilon_i-\Omega+z_3)}\Bigg].
\end{aligned} \tag{2.28}$$

The analytic continuation procedure then requires us to take the following limits

$$\begin{aligned}
z_1 &\to -\omega_i - i0^+, \\
z_2 &\to \omega_f + i0^+, \\
z_3 &\to -\omega_f' + i0^+, \\
z_4 &\to \omega_i' - i0^+
\end{aligned} \tag{2.29}$$

and then take the limit

$$\omega_i' - \omega_i = \omega_f' - \omega_f \to 0 \tag{2.30}$$

in order to reproduce an expression proportional to the resonant scattering cross section in Eq. (2.9). The final general expression for the resonant scattering becomes

$$R_R(\boldsymbol{q},\Omega) = \frac{2\pi g^2(\boldsymbol{k}_i)g^2(\boldsymbol{k}_f)}{1-\exp(-\beta\Omega)}\chi_R(\boldsymbol{q},\Omega) \tag{2.31}$$

with the resonant Raman response function defined by

$$\chi_R(\boldsymbol{q},\Omega) = \frac{1}{2\pi i}\left\{\chi^{(4)}_{i,f,f,i}(z_1,z_2,z_3,z_4)\Bigg|^{z_3+z_4=-z_1-z_2\to\Omega+i0^+}_{z_3+z_4=-z_1-z_2\to\Omega-i0^+}\right\}\Bigg|_{\substack{z_1\to-\omega_i-i0^+\\ z_2\to\omega_f+i0^+\\ z_3\to-\omega_f'+i0^+\\ z_4\to\omega_i'-i0^+}}\Bigg|_{\substack{\omega_i'-\omega_i\to0\\ \omega_f'-\omega_f\to0}}. \tag{2.32}$$

Note that it is critical to perform the analytic continuation of $z_3 + z_4 = -z_1 - z_2 \to \Omega \pm i0^+$ first and then analytically continue the other frequencies [as in Eq. (2.28) and (2.29)] since these procedures do not commute with one another.

III. EXACT RESULTS FOR THE FALICOV-KIMBALL MODEL

We now evaluate the general expressions derived above for the case of optical Raman scattering, where all momenta vanish ($\boldsymbol{k}_i = \boldsymbol{k}_f = \boldsymbol{q} = 0$) and for the spinless Falicov-Kimball model. The Falicov-Kimball model involves the interaction of conduction electrons with localized electrons and has the following Hamiltonian[24]

$$\begin{aligned}
H = &-\frac{t^*}{2\sqrt{D}}\sum_{\langle i,j\rangle}(c_i^\dagger c_j + c_j^\dagger c_i) + E_f\sum_i w_i - \mu\sum_i(c_i^\dagger c_i + w_i) \\
&+ U\sum_i c_i^\dagger c_i w_i,
\end{aligned} \tag{3.1}$$

where $c_i^\dagger$ (c_i) create (destroy) a conduction electron at site i, w_i is a classical variable (representing the localized electron number at site i) that equals 0 or 1, t^* is a renormalized hopping matrix that is nonzero between nearest neighbors on a hypercubic lattice in D-dimensions (and we take the limit $D \to \infty$), and U is the local screened Coulomb interaction between conduction and localized electrons. $\langle i,j\rangle$ denotes a sum over sites i and nearest neighbors j. E_f and μ are adjusted to set the average filling of conduction and localized

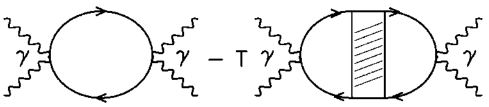

FIG. 1. Feynman diagrams for nonresonant Raman scattering. The wavy lines denote photon propagators and the solid lines denote electron propagators. The cross-hatched rectangle is the *reducible* charge vertex. In the B_{1g} channel, only the bare (first) diagram enters, while in the A_{1g} channel both diagrams enter. The symbol γ denotes the stress-tensor vertex of the corresponding electron-photon interaction.

electrons. In our calculations the average filling for each is set to 1/2, respectively ($\mu = U/2, E_f = 0$).

This model can be solved exactly by using DMFT, as first described by Brandt and Mielsch.[26] The algorithm used to solve for the local Green's function at site i, defined by

$$G_i(\tau) = -\langle \mathcal{T}_\tau c_i(\tau) c_i^\dagger(0)\rangle, \tag{3.2}$$

where the angle brackets denote the trace weighted by the Boltzmann factor $\exp[-\beta H]/\mathcal{Z}$. We usually work with the Fourier transform of the imaginary-time Green's function to yield the Matsubara frequency Green's function. The momentum-dependent Green's function becomes

$$G_m(\boldsymbol{k}) = \frac{1}{Z_m - \epsilon_k}, \tag{3.3}$$

with

$$\epsilon_k = -\lim_{D\to\infty} \frac{t^*}{\sqrt{D}} \sum_{\alpha=1}^{D} \cos k_\alpha \tag{3.4}$$

being the noninteracting band energy, and

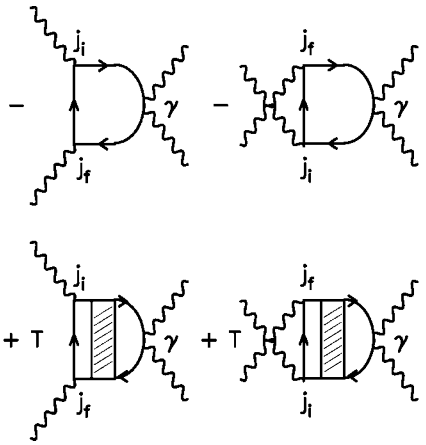

FIG. 2. Feynman diagrams for the mixed contributions to Raman scattering. The symbols j_f and j_i remind us to include the relevant vertex factors from the current operator in the electron-photon interaction. The mixed contribution vanishes in the B_{2g} channel, it consists of only the bare diagrams on the top line in the B_{1g} channel (and turns out to be a $1/D$ correction), and all diagrams enter for the A_{1g} channel.

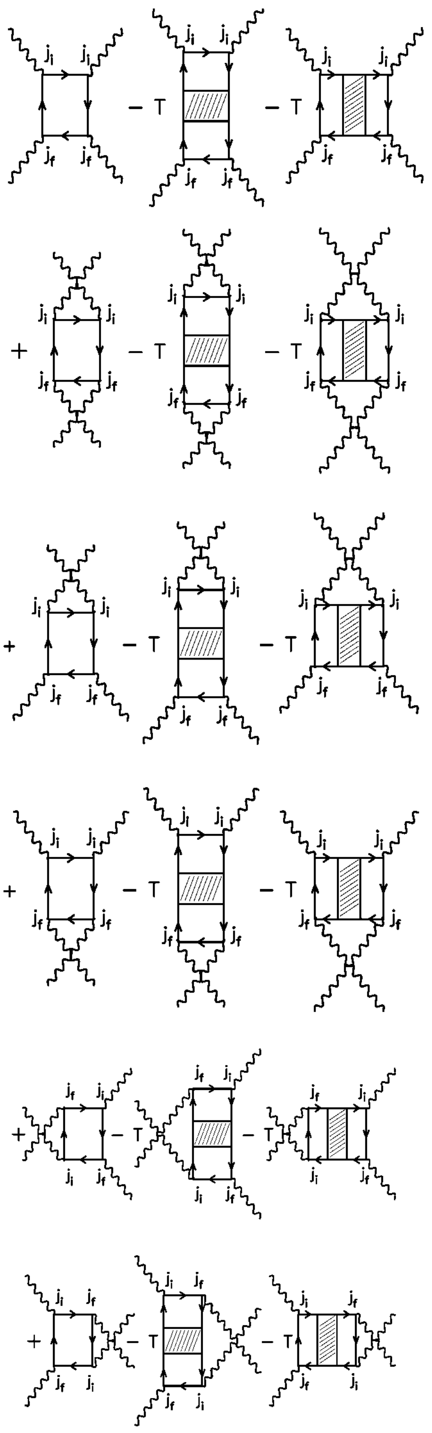

FIG. 3. Feynman diagrams for the resonant contributions to Raman scattering. Only the first two diagrams in the first four lines, and the first diagram in the last two lines contribute in the B_{1g} and B_{2g} sectors. The A_{1g} response includes all diagrams.

$$Z_m = i\omega_m + \mu - \Sigma_m. \tag{3.5}$$

The local self-energy Σ_m is a solution of the following set of equations:

$$G_m = \frac{1}{N}\sum_k \frac{1}{Z_m - \epsilon_k} = \frac{1}{Z_m - \lambda_m} = \frac{w_1}{i\omega_m + \mu - \lambda_m - U} + \frac{1 - w_1}{i\omega_m + \mu - \lambda_m}, \tag{3.6}$$

where we introduced the self-consistent dynamical mean-field of Brandt and Mielsch (denoted λ); the self-energy can be expressed as a simple function of this field

$$\Sigma_m = Uw_1 + \frac{U^2 w_1(1 - w_1)}{i\omega_m + \mu - \lambda_m - U(1 - w_1)}. \tag{3.7}$$

Here w_1 is given by $w_1 = e^{[-\beta(E_f - \mu)]}\mathcal{Z}_0(U-\mu)/\mathcal{Z}$, with $\mathcal{Z}_0(\mu) = 2e^{\beta\mu/2}\prod_{n=-\infty}^{\infty}(i\omega_n - \mu - \lambda_n)/i\omega_n$.

A. Nonresonant scattering

The case of nonresonant Raman scattering was considered by two of us,[7] so we only sketch the derivation to show our notation and to present the final results. In general, the two-time correlation function in Eq. (2.13), constructed from the stress operators, can be represented by the summation of a generalized "polarization"

$$\chi^{(2)}_{\tilde{\gamma},\tilde{\gamma}}(-i\nu, i\nu) = T\sum_m \Pi(i\omega_m, i\omega_{m+\nu}), \tag{3.8}$$

where we use a shorthand notation $i\omega_{m+\nu} = i\omega_m + i\nu$ and $G_{m+\nu} = G(i\omega_{m+\nu}) = G(i\omega_m + i\nu)$ and similarly for Σ and Z. A tedious calculation shows that[7]

$$\Pi(i\omega_m, i\omega_{m+\nu}) = -\frac{t^{*2}}{2}\frac{G_m - G_{m+\nu}}{Z_{m+\nu} - Z_m} \tag{3.9}$$

in the B_{1g} channel and

$$\Pi(i\omega_m, i\omega_{m+\nu}) = -\frac{1}{i\nu}\frac{\Sigma_m - \Sigma_{m+\nu}}{G^{-1}_{m+\nu} - G^{-1}_m}(Z_{m+\nu} - Z_m) \tag{3.10}$$

in the A_{1g} channel (see Fig. 1 for the relevant Feynman diagrams).

Since one can show that there are no additional singularities or nonanalyticities in Eqs. (3.9) and (3.10) connected with the denominators,[27] one can directly perform the analytic continuation and replace the sum over Matsubara frequencies in Eq. (3.8) by an integral over the real axis

$$\chi^{(2)}_{\tilde{\gamma},\tilde{\gamma}}(-i\nu, i\nu) = \frac{1}{2\pi i}\int_{-\infty}^{+\infty} d\omega f(\omega)[\Pi(\omega - i0^+, \omega + i\nu) - \Pi(\omega + i0^+, \omega + i\nu) + \Pi(\omega - i\nu, \omega - i0^+) - \Pi(\omega - i\nu, \omega + i0^+)], \tag{3.11}$$

where $f(\omega) = 1/[1 + \exp(\beta\omega)]$ is the Fermi distribution function. After substituting Eq. (3.11) into the expression for the nonresonant response function in Eq. (2.15), we obtain

$$\chi_N(\Omega) = \frac{2}{(2\pi i)^2}\int_{-\infty}^{+\infty} d\omega[f(\omega) - f(\omega + \Omega)] \times \mathrm{Re}\{\Pi(\omega - i0^+, \omega + \Omega + i0^+) - \Pi(\omega - i0^+, \omega + \Omega - i0^+)\}. \tag{3.12}$$

Now we can take the trivial analytic continuation of Eqs. (3.9) and (3.10) to find the final expressions for the nonresonant Raman response function:

$$\chi_{N,B_{1g}}(\Omega) = \frac{t^{*2}}{4\pi^2}\int_{-\infty}^{+\infty} d\omega[f(\omega) - f(\omega + \Omega)] \times \mathrm{Re}\left\{\frac{G(\omega) - G^*(\omega + \Omega)}{Z^*(\omega + \Omega) - Z(\omega)} - \frac{G(\omega) - G(\omega + \Omega)}{Z(\omega + \Omega) - Z(\omega)}\right\} \tag{3.13}$$

in the B_{1g} channel, and

$$\chi_{N,A_{1g}}(\Omega) = \frac{1}{2\pi^2\Omega}\int_{-\infty}^{+\infty} d\omega[f(\omega) - f(\omega + \Omega)] \times \mathrm{Re}\left\{\frac{[\Sigma(\omega) - \Sigma^*(\omega + \Omega)][Z^*(\omega + \Omega) - Z(\omega)]}{G^{-1*}(\omega + \Omega) - G^{-1}(\omega)} - \frac{[\Sigma(\omega) - \Sigma(\omega + \Omega)][Z(\omega + \Omega) - Z(\omega)]}{G^{-1}(\omega + \Omega) - G^{-1}(\omega)}\right\} \tag{3.14}$$

in the A_{1g} channel, respectively.

B. Mixed scattering

The mixed Raman response corresponds to the scattering processes that involve three external vertices: one stress tensor and two current operators, and there are two types of diagrams corresponding to the direct and exchange processes (see Fig. 2). There is no mixed Raman response for the B_{2g} channel because the stress tensor vanishes for the case of nearest neighbor hopping only. In the B_{1g} channel it appears to be only a bare response (we will see below that it actually vanishes) and for the A_{1g} channel, the bare mixed response is renormalized by the irreducible charge vertex.

1. B_{1g} channel

In the B_{1g} channel, the mixed Raman response contains only the bare direct and exchange contributions (first two terms in Fig. 2, respectively):

$$\chi^{(3)}_{\tilde{\gamma},f,i}(i\nu_i - i\nu_f, i\nu_f, -i\nu_i) = T\sum_m \frac{1}{N}\sum_k \frac{t^{*3}}{D^{3/2}}\sum_{\alpha=1}^{D}(-1)^\alpha \cos k_\alpha \times \sum_{\beta=1}^{D}(-1)^\beta \sin k_\beta \sum_{\gamma=1}^{D}\sin k_\gamma \times [G_m(\boldsymbol{k})G_{m-\nu_f}(\boldsymbol{k})G_{m+\nu_i-\nu_f}(\boldsymbol{k}) + G_m(\boldsymbol{k})G_{m+\nu_f}(\boldsymbol{k})G_{m-\nu_i+\nu_f}(\boldsymbol{k})], \tag{3.15}$$

because the symmetry of all two and three-particle vertices is that of the lattice (A_{1g}), so all renormalizations vanish (recall the current operator has odd parity, whereas $\epsilon_{\boldsymbol{k}}$ is even in $\boldsymbol{k}$). The expression in Eq. (3.15) has nonzero values only when the subscripts are equal $\alpha=\beta=\gamma$. In this case, we expand the product of Green's functions into partial fractions over $\epsilon_{\boldsymbol{k}}$ and the summations over momentum involve only expressions of the type [$\zeta_m=-\mathrm{sgn}(\mathrm{Im}\,Z_m)$]:

$$\begin{aligned}\frac{1}{N}\sum_k \frac{t^{*3}}{D^{3/2}}\sum_{\alpha=1}^{D} \cos k_\alpha \sin^2 k_\alpha \frac{1}{Z_m-\epsilon_k} &= \frac{it^{*3}}{\sqrt{D}}\int_0^{\zeta_m\infty} d\lambda e^{-i\lambda Z_m} J_0^{D-1}\left(\frac{\lambda t^*}{\sqrt{D}}\right)\\ &\times \int_{-\pi}^{\pi}\frac{dk}{2\pi}\sin^2 k \cos k e^{i(\lambda t^*/\sqrt{D})\cos k} \qquad (3.16)\end{aligned}$$

with J_0 being Bessel's function. The last exponent is expanded in a power series over $\lambda t^*/\sqrt{D}$ that yields in the $D\to\infty$ limit

$$\begin{aligned}&\lim_{D\to\infty} -\frac{t^{*4}}{8D}\frac{d}{dZ_m}\left[i\zeta_m\frac{\sqrt{\pi}}{t^*}e^{-Z_m^2/t^{*2}}\,\mathrm{erfc}\left(i\zeta_m\frac{Z_m}{t^*}\right)\right]\\ &= \lim_{D\to\infty}\frac{t^{*2}}{4D}(Z_mG_m-1)\to 0 \qquad (3.17)\end{aligned}$$

so the mixed contribution vanishes in the B_{1g} channel.

2. A_{1g} channel

In the A_{1g} channel, the mixed Raman response contains both bare and renormalized contributions:

$$\begin{aligned}&\chi^{(3)}_{\tilde{\gamma},f,i}(i\nu_i-i\nu_f,i\nu_f,-i\nu_i)\\ &= T\sum_m\Bigg\{-\frac{1}{N}\sum_k \epsilon_k\frac{t^{*2}}{D}\sum_{\alpha=1}^{D}\sin k_\alpha\sum_{\beta=1}^{D}\sin k_\beta G_m(\boldsymbol{k})G_{m-\nu_f}(\boldsymbol{k})\\ &\times G_{m+\nu_i-\nu_f}(\boldsymbol{k}) - \frac{1}{N}\sum_k\frac{t^{*2}}{D}\sum_{\alpha,\beta=1}^{D}\sin k_\alpha \sin k_\beta\\ &\times G_m(\boldsymbol{k})G_{m-\nu_f}(\boldsymbol{k})G_{m+\nu_i-\nu_f}(\boldsymbol{k})\\ &\times T\tilde{\Gamma}(i\omega_m,i\omega_m+i\nu_i-i\nu_f)\times\frac{1}{N}\sum_k\epsilon_kG_m(\boldsymbol{k})G_{m+\nu_i-\nu_f}(\boldsymbol{k})\Bigg\}\\ &+\begin{bmatrix} i\nu_i\to -i\nu_i\\ i\nu_f\to -i\nu_f\end{bmatrix}. \qquad (3.18)\end{aligned}$$

The renormalizations are only with respect to two-particle vertices, because the current operators are odd in parity and cannot be renormalized by a local three-particle vertex. Here

$$\begin{aligned}&\tilde{\Gamma}(i\omega_m,i\omega_m+i\nu_i-i\nu_f)\\ &= \frac{\Gamma(i\omega_m,i\omega_m+i\nu_i-i\nu_f)}{1-T\Gamma(i\omega_m,i\omega_{m+\nu_i-\nu_f})\frac{1}{N}\sum_k G_m(\boldsymbol{k})G_{m+\nu_i-\nu_f}(\boldsymbol{k})} \qquad (3.19)\end{aligned}$$

is the total (reducible) charge vertex. In the $D=\infty$ Falicov-Kimball model, the irreducible charge vertex satisfies

$$\Gamma(i\omega_m,i\omega_m+i\nu)=\frac{1}{T}\frac{\Sigma_m-\Sigma_{m+\nu}}{G_m-G_{m+\nu}} \qquad (3.20)$$

on the Matsubara frequency axis.[27] Substituting into the expression for the reducible charge vertex gives

$$\begin{aligned}\tilde{\Gamma}(i\omega_m,i\omega_{m+\nu_i-\nu_f}) &= \frac{1}{T}\frac{Z_{m+\nu_i-\nu_f}-Z_m}{i\nu_i-i\nu_f}\frac{\Sigma_m-\Sigma_{m+\nu_i-\nu_f}}{G_m-G_{m+\nu_i-\nu_f}}\\ &= \frac{1}{T}\Bigg(\frac{Z_m-Z_{m+\nu_i-\nu_f}}{G_m-G_{m+\nu_i-\nu_f}}\\ &+\frac{(Z_{m+\nu_i-\nu_f}-Z_m)^2}{(i\nu_i-i\nu_f)(G_m-G_{m+\nu_i-\nu_f})}\Bigg). \qquad (3.21)\end{aligned}$$

Now Eq. (3.18) has nonzero values only when $\alpha=\beta$ and, noting that in the $D\to\infty$ limit one can replace $\sin^2 k_\alpha$ by its average value $\frac{1}{2}$, yields

$$\begin{aligned}\chi^{(3)}_{\tilde{\gamma},f,i}(i\nu_i-i\nu_f,i\nu_f,-i\nu_i) &= T\sum_m[\Pi^{(3)}(i\omega_m-i\nu_f,i\omega_m+i\nu_i\\ &-i\nu_f,i\omega_m)+\Pi^{(3)}(i\omega_m+i\nu_i,i\omega_m\\ &+i\nu_i-i\nu_f,i\omega_m)], \qquad (3.22)\end{aligned}$$

where

$$\begin{aligned}&\Pi^{(3)}(i\omega_m-i\nu_f,i\omega_m+i\nu_i-i\nu_f,i\omega_m)\\ &= \frac{t^{*2}}{2(i\nu_i-i\nu_f)}\frac{\Sigma_m-\Sigma_{m+\nu_i-\nu_f}}{G_m-G_{m+\nu_i-\nu_f}}\\ &\times\left[G_{m+\nu_i-\nu_f}\frac{G_m-G_{m-\nu_f}}{Z_{m-\nu_f}-Z_m}-G_m\frac{G_{m+\nu_i-\nu_f}-G_{m-\nu_f}}{Z_{m-\nu_f}-Z_{m+\nu_i-\nu_f}}\right]. \qquad (3.23)\end{aligned}$$

In the case when there are neither singularities nor nonanalyticities in Eq. (3.23) connected with the denominators, one can trivially perform the analytic continuation and replace the sum over Matsubara frequencies in Eq. (3.22) by an integral over the real axis. We only keep the eight terms that contain the difference $i\nu_i-i\nu_f$ and hence contribute to the mixed scattering. Substituting into Eq. (2.22)(with the sign of the arguments of the first two terms inverted) we get the final expression:

$$\chi_{M,A_{1\mathrm{g}}}(\Omega) = \frac{2}{(2\pi i)^2}\int_{-\infty}^{+\infty} d\omega[f(\omega) - f(\omega+\Omega)]\sum_{\eta=\pm} \mathrm{Re}\{\eta\Pi^{(3)}(\omega-\omega_f+i0^+,\omega+\Omega+\eta i0^+,\omega-i0^+) + \eta\Pi^{(3)}(\omega-\omega_f-i0^+,\omega+\Omega + \eta i0^+,\omega-i0^+) + \eta\Pi^{(3)}(\omega+\omega_i-i0^+,\omega+\Omega+\eta i0^+,\omega-i0^+) + \eta\Pi^{(3)}(\omega+\omega_i+i0^+,\omega+\Omega+\eta i0^+,\omega-i0^+)\}. \quad (3.24)$$

Here the analytic continuation of Eq. (3.23) is

$$\Pi^{(3)}(\omega_1,\omega_2,\omega_3) = \frac{t^{*2}}{2(\omega_2-\omega_3)}\frac{\Sigma(\omega_3)-\Sigma(\omega_2)}{G(\omega_3)-G(\omega_2)}\left[G(\omega_2)\frac{G(\omega_3)-G(\omega_1)}{Z(\omega_1)-Z(\omega_3)} - G(\omega_3)\frac{G(\omega_2)-G(\omega_1)}{Z(\omega_1)-Z(\omega_2)}\right]. \quad (3.25)$$

C. Resonant scattering

The resonant Raman response corresponds to scattering processes that involve four external current vertices. The correlation function constructed from four current operators contains six types of diagrams corresponding to the different direct and exchange processes (see Fig. 3). It should be noted that since $j^{(i)}$ and $j^{(f)}$ are odd functions of momentum, the only way to get a nonzero momentum summation is to have an even number of current operators in any given momentum integration ("current-operator pairing"). Hence all local three-particle and four-particle vertex renormalizations must vanish, although two-particle vertex renormalizations are possible. For the B_{1g} and B_{2g} channels the "current-operator pairing" is possible only between either both incoming $j^{(i)}$ or both final $j^{(f)}$ current operators, but for the A_{1g} channel all operators can be involved in the "pairing" and the contribution from the bare diagrams in the A_{1g} channel is three times larger than for the B_{1g} channel. As a result, in the B_{1g} and B_{2g} channels we have contributions from the first two diagrams in the first four lines and from only the first diagram in the last two lines of Fig. 3, and in the A_{1g} channel all diagrams contribute.

For the B_{1g} and B_{2g} channels, the product $j^{(i)}j^{(f)}$ is orthogonal to the charge vertex with A_{1g} symmetry, so the diagrams are not renormalized across the vertices that contain both $j^{(i)}$ and $j^{(f)}$ factors. In addition, for the B_{2g} channel, the polarization vectors select either odd or even momentum coordinates and, as a result, the resonant Raman response for the B_{2g} channel is four times smaller than for the B_{1g} one, and it is the only contribution to the total Raman response in the B_{2g} channel. In the A_{1g} channel, besides the diagrams presented in Fig. 3 that include all possible horizontal and vertical "ladder" renormalizations, one could renormalize by parquet-like terms that involve simultaneous horizontal and vertical renormalizations. But it can be shown (see the Appendix), that such contributions are $1/D$ corrections, and disappear in the $D\to\infty$ limit.

As a result, the Fourier transform of the four-time correlation function constructed from the current operators can be represented in the following form ($i\nu_i - i\nu_f = i\nu_i' - i\nu_f'$):

$$\begin{aligned}\chi^{(4)}_{i,f,f,i}(-i\nu_i,i\nu_f,-i\nu_f',i\nu_i') = T\sum_m [&\Pi_I^{(4)}(i\omega_m,i\omega_m-i\nu_f,i\omega_m+i\nu_i-i\nu_f,i\omega_m-i\nu_f')\\ &+\Pi_I^{(4)}(i\omega_m,i\omega_m+i\nu_f',i\omega_m-i\nu_i+i\nu_f,i\omega_m+i\nu_f)+\Pi_I^{(4)}(i\omega_m,i\omega_m-i\nu_f,i\omega_m-i\nu_f'-i\nu_f,i\omega_m-i\nu_f')\\ &+\Pi_I^{(4)}(i\omega_m,i\omega_m+i\nu_f',i\omega_m+i\nu_i+i\nu_f',i\omega_m+i\nu_f)+\Pi_{II}^{(4)}(i\omega_m,i\omega_m+i\nu_i,i\omega_m+i\nu_i-i\nu_f,i\omega_m-i\nu_f')\\ &+\Pi_{II}^{(4)}(i\omega_m,i\omega_m-i\nu_f,i\omega_m+i\nu_i-i\nu_f,i\omega_m+i\nu_i')].\end{aligned} \quad (3.26)$$

In the B_{1g} and B_{2g} channels, $\Pi_{II}^{(4)}$ contains only the bare contribution (corresponding to only the first diagram on last two lines of Fig. 3)

$$\Pi^{(4)}_{II,B_{1g}}(i\omega_1,i\omega_2,i\omega_3,i\omega_4) = \Pi^{(4)}_{\mathrm{bare}}(i\omega_1,i\omega_2,i\omega_3,i\omega_4), \quad (3.27)$$

$$\Pi^{(4)}_{II,B_{2g}}(i\omega_1,i\omega_2,i\omega_3,i\omega_4) = \frac{1}{4}\Pi^{(4)}_{II,B_{1g}}(i\omega_1,i\omega_2,i\omega_3,i\omega_4),$$

where

$$\Pi^{(4)}_{\text{bare}}(i\omega_1,i\omega_2,i\omega_3,i\omega_4) = -\frac{t^{*4}}{D^2}\frac{1}{N}\sum_{\boldsymbol{k}} \frac{\sum_{\alpha=1}^{D}\sin^2 k_\alpha \sum_{\beta=1}^{D}\sin^2 k_\beta}{(Z_1-\epsilon_{\boldsymbol{k}})(Z_2-\epsilon_{\boldsymbol{k}})(Z_3-\epsilon_{\boldsymbol{k}})(Z_4-\epsilon_{\boldsymbol{k}})} = -\frac{t^{*4}}{4}\left[\frac{G_1}{(Z_2-Z_1)(Z_3-Z_1)(Z_4-Z_1)} + \frac{G_2}{(Z_1-Z_2)(Z_3-Z_2)(Z_4-Z_2)} + \frac{G_3}{(Z_1-Z_3)(Z_2-Z_3)(Z_4-Z_3)} + \frac{G_4}{(Z_1-Z_4)(Z_2-Z_4)(Z_3-Z_4)}\right]. \tag{3.28}$$

However, the other polarization $\Pi^{(4)}_I$ contains a vertical “ladder” renormalization (corresponding to the first two diagrams on the first four lines of Fig. 3)

$$\Pi^{(4)}_{I,B_{1g}}(i\omega_1,i\omega_2,i\omega_3,i\omega_4) = \Pi^{(4)}_{\text{bare}}(i\omega_1,i\omega_2,i\omega_3,i\omega_4) + \Pi^{(4)}_{\text{r}}(i\omega_1,i\omega_2,i\omega_3,i\omega_4), \tag{3.29}$$

$$\Pi^{(4)}_{I,B_{2g}}(i\omega_1,i\omega_2,i\omega_3,i\omega_4) = \frac{1}{4}\Pi^{(4)}_{I,B_{1g}}(i\omega_1,i\omega_2,i\omega_3,i\omega_4)$$

with

$$\Pi^{(4)}_{\text{r}}(i\omega_1,i\omega_2,i\omega_3,i\omega_4) = -T\left(\frac{1}{N}\sum_{\boldsymbol{k}}\frac{t^{*2}}{D}\sum_{\alpha=1}^{D}\sin^2 k_\alpha G_1(\boldsymbol{k})G_2(\boldsymbol{k})G_4(\boldsymbol{k})\right)\Gamma(2,4)\left(\frac{1}{N}\sum_{\boldsymbol{k}}\frac{t^{*2}}{D}\sum_{\alpha=1}^{D}\sin^2 k_\alpha G_2(\boldsymbol{k})G_4(\boldsymbol{k})G_3(\boldsymbol{k})\right) = -T\frac{t^{*4}}{4}\left(\frac{G_4-G_1}{Z_1-Z_4}-\frac{G_2-G_1}{Z_1-Z_2}\right)\frac{\tilde{\Gamma}(2,4)}{(Z_2-Z_4)^2}\left(\frac{G_4-G_3}{Z_3-Z_4}-\frac{G_2-G_3}{Z_3-Z_2}\right). \tag{3.30}$$

Using the solution of Eq. (3.21) in the Bethe-Salpeter-like equation (3.19) yields

$$\Pi^{(4)}_{\text{r}}(i\omega_1,i\omega_2,i\omega_3,i\omega_4) = \tilde{\Pi}^{(4)}_{\text{r}}(i\omega_1,i\omega_2,i\omega_3,i\omega_4) + \frac{\Psi^{(4)}_{\text{r}}(i\omega_1,i\omega_2,i\omega_3,i\omega_4)}{i\omega_2-i\omega_4}, \tag{3.31}$$

with

$$\tilde{\Pi}^{(4)}_{\text{r}}(i\omega_1,i\omega_2,i\omega_3,i\omega_4) = \frac{t^{*4}}{4}\frac{1}{(G_2-G_4)(Z_2-Z_4)}\left(\frac{G_4-G_1}{Z_1-Z_4}-\frac{G_2-G_1}{Z_1-Z_2}\right)\left(\frac{G_4-G_3}{Z_3-Z_4}-\frac{G_2-G_3}{Z_3-Z_2}\right), \tag{3.32}$$

and

$$\Psi^{(4)}_{\text{r}}(i\omega_1,i\omega_2,i\omega_3,i\omega_4) = -\frac{t^{*4}}{4}\frac{1}{G_2-G_4}\left(\frac{G_4-G_1}{Z_1-Z_4}-\frac{G_2-G_1}{Z_1-Z_2}\right)\left(\frac{G_4-G_3}{Z_3-Z_4}-\frac{G_2-G_3}{Z_3-Z_2}\right) = \Psi^{(4)}_{\text{r}}(i\omega_3,i\omega_2,i\omega_1,i\omega_4) = -\Psi^{(4)}_{\text{r}}(i\omega_1,i\omega_4,i\omega_3,i\omega_2). \tag{3.33}$$

In the A_{1g} channel we have contributions from all the diagrams in Fig. 3, hence

$$\Pi^{(4)}_{I,A_{1g}}(i\omega_1,i\omega_2,i\omega_3,i\omega_4) = \Pi^{(4)}_{II,A_{1g}}(i\omega_1,i\omega_2,i\omega_3,i\omega_4) = 3\Pi^{(4)}_{\text{bare}}(i\omega_1,i\omega_2,i\omega_3,i\omega_4) + \Pi^{(4)}_{\text{r}}(i\omega_1,i\omega_2,i\omega_3,i\omega_4) + \Pi^{(4)}_{\text{r}}(i\omega_2,i\omega_3,i\omega_4,i\omega_1). \tag{3.34}$$

Here the last term corresponds to the horizontal “ladder” renormalization (the last diagram on each line of Fig. 3).

Next, we perform the analytic continuation in Eq. (3.26) and replace the sum over Matsubara frequencies by an integral over the real axis in the same way as was done in Eq. (3.24) for the mixed scattering. Then we substitute it into the expression in Eq. (3.32) for the resonant Raman response. After some tedious algebra, we achieve the final expression for the resonant Raman response of the $D=\infty$ Falicov-Kimball model:

$$\chi_R(\Omega) = \frac{2}{(2\pi i)^2}\int_{-\infty}^{+\infty} d\omega[f(\omega)-f(\omega+\Omega)]\sum_{\eta=\pm}\text{Re}\{\eta\Pi^{(4)}_I(\omega-i0^+,\omega-\omega_f-i0^+,\omega+\Omega+\eta i0^+,\omega-\omega_f+i0^+) + \eta\Pi^{(4)}_I(\omega-i0^+,\omega+\omega_i-i0^+,\omega+\Omega+\eta i0^+,\omega+\omega_i+i0^+) + \eta\Pi^{(4)}_{II}(\omega-i0^+,\omega+\omega_i+i0^+,\omega+\Omega+\eta i0^+,\omega-\omega_f+i0^+) + \eta\Pi^{(4)}_{II}(\omega-i0^+,\omega+\omega_i-i0^+,\omega+\Omega+\eta i0^+,\omega-\omega_f-i0^+)\}. \tag{3.35}$$

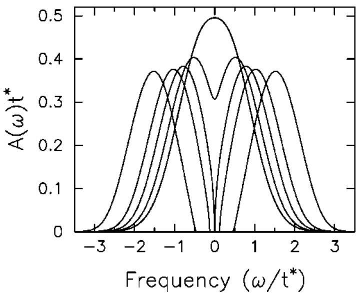

FIG. 4. Interacting single-particle density of states for $U=0.5$, 1.0, 1.5, 2.0, and 3.0 (U increases as the pseudogap becomes stronger). Note how the DOS first develops a depression near the chemical potential and then develops a pseudogap as the metal-insulator transition occurs (the DOS vanishes only at $\omega=0$ in the insulator).

The analytic continuation in Eq. (3.35) can be found simply by substituting $i\omega_\alpha \to \omega_\alpha \pm i0^+$ in the corresponding expressions in Eqs. (3.27)–(3.34) which will not be explicitly repeated here. It might appear that "polarizations" $\Pi_I^{(4)}$ contain divergences connected with vanishing denominators in the last term in Eq. (3.31), but the contribution of these terms into the expression in braces in Eq. (3.35) must be considered in the limit:

$$\begin{aligned}\lim_{\Delta\to 0}\frac{1}{2\Delta}\sum_{\eta=\pm 1}\{&\eta\Psi_{\mathrm{r}}^{(4)}(\omega-\eta i0^+,\omega-\omega_f-i0^+,\omega+\Omega+i0^+,\omega\\&-\omega_f-\Delta+i0^+)+\eta\Psi_{\mathrm{r}}^{(4)}(\omega+\eta i0^+,\omega-\omega_f-i0^+,\omega+\Omega\\&-i0^+,\omega-\omega_f-\Delta+i0^+)+\eta\Psi_{\mathrm{r}}^{(4)}(\omega-\eta i0^+,\omega+\omega_i+\Delta-i0^+,\omega\\&+\Omega+i0^+,\omega+\omega_i+i0^+)+\eta\Psi_{\mathrm{r}}^{(4)}(\omega+\eta i0^+,\omega+\omega_i+\Delta-i0^+,\omega\\&+\Omega-i0^+,\omega+\omega_i+i0^+)\},\end{aligned} \tag{3.36}$$

where $\Delta=\omega_f'-\omega_f=\omega_i'-\omega_i$. When the limit $\Delta\to 0$ is taken, we find that the imaginary part of Eq. (3.36) diverges, but the real part (which is all that contributes to the Raman scattering) is finite and can be calculated analytically using l'Hopital's rule; one must do this carefully in the insulating phase where the self-energy develops a pole.

D. Bare contributions and multiple resonances

In summary, the total Raman response function is the sum of the nonresonant [Eq. (3.12)], mixed [Eq. (3.24)], and resonant [Eq. (3.35)] contributions and has a complicated form. It is educational to consider the contributions of the bare diagrams, which can be summed up and rewritten in the following form:[28]

$$\begin{aligned}\chi(\Omega)=\frac{1}{N}\sum_{\boldsymbol{k}}\int_{-\infty}^{+\infty}&d\omega[f(\omega)-f(\omega+\Omega)]A_{\boldsymbol{k}}(\omega)A_{\boldsymbol{k}}(\omega+\Omega)\\&\times|\gamma_{\boldsymbol{k}}+v_{\boldsymbol{k}}^i v_{\boldsymbol{k}}^f[G_{\boldsymbol{k}}(\omega+\omega_i+i0^+)+G_{\boldsymbol{k}}(\omega-\omega_f-i0^+)]|^2,\end{aligned} \tag{3.37}$$

where $\gamma_{\boldsymbol{k}}=\Sigma_{\alpha,\beta}e_\alpha^i(\partial^2\varepsilon_{\boldsymbol{k}}/\partial\boldsymbol{k}_\alpha\partial\boldsymbol{k}_\beta)e_\beta^f$, $v_{\boldsymbol{k}}^{i,f}=\Sigma_\alpha e_\alpha^{i,f}(\partial\varepsilon_{\boldsymbol{k}}/\partial k_\alpha)$, $A_{\boldsymbol{k}}(\omega)=(1/\pi)\mathrm{Im}\,G_{\boldsymbol{k}}(\omega-i0^+)$, and

$$G_{\boldsymbol{k}}(\omega)=\frac{1}{\omega+\mu-\Sigma(\omega)-\epsilon_{\boldsymbol{k}}} \tag{3.38}$$

is the momentum-dependent Green's function.

In general, the bare response function in Eq. (3.37) is a function of the frequency shift $\Omega=\omega_i-\omega_f$, of the incoming photon frequency ω_i and the outgoing photon frequency ω_f; it can be enhanced when one or both of the denominators are resonant (i.e., they coincide). In the latter case, we have a so-called "double" or "multiple resonance."[30] The full response function also includes the vertex renormalizations. But the total (reducible) charge vertex in Eq. (3.21) for the Falicov-Kimball model does not diverge, and hence it does not introduce any additional "resonances." It only leads to a renormalization of the total Raman response.

IV. NUMERICAL RESULTS

We begin our results by showing the single particle density of states of the spinless Falicov-Kimball model in infinite dimensions with $\langle\rho_e\rangle=\langle w_i\rangle=1/2$. The density of states is independent of temperature, and a metal-insulator transition occurs at $U=\sqrt{2}$. In the insulating phase, the self-energy develops a pole at $\omega=0$, and the Green's function vanishes there. There is no true gap to this system, as the bare Gaussian density of states forces the interacting density of states to be nonzero whenever the self-energy is finite.[31] In Fig. 4, we plot the DOS for 5 values of U ranging from a weakly scattering metal $U=0.5$, to a strongly scattering metal $U=1$, to a near-critical insulator $U=1.5$, a "small-gap"-insulator $U=2$ and a "moderate-gap"-insulator $U=3$. Note that the metal-insulator transition is continuous for the Falicov-Kimball model, in the sense that the zero-temperature dc conductivity continuously goes to zero at the transition. Note further that in the metallic phase, the system is not a Fermi liquid because the scattering time at the putative Fermi surface does not become infinite as $T\to 0$.

A fundamental question is to the size of the energy scales in the system. Normally one would take the hopping t^* to be on the order of 0.25 to 4 eV for a general correlated system. In this case, room temperature would range from 0.006 to 0.1 (depending on the actual value of t^*). The hopping scale can be reduced, however, if we do not view it as the microscopic scale, but instead view it as describing a renormalized low-energy band, which is further correlated by the Falicov-Kimball interaction term. In that case, we would adjust the hopping to produce the bandwidth of the actual strongly correlated bands of the system, which could result in a lower value for t^* in eV.

Once the self-energy and the DOS are known, the different contributions to Raman scattering can be determined by straightforward, but tedious numerical integrations of the relevant functions for each scattering channel [Eqs. (3.13), (3.14), (3.24), (3.25), (3.35), and (3.36)]. There are some subtleties with this approach, especially in the insulating phase, as the iterative approach to determining the DOS and the self energy becomes inaccurate once the imaginary part of the self energy becomes smaller than about 10^{-13}. Fortunately, there is a simple analytic form that can be used to

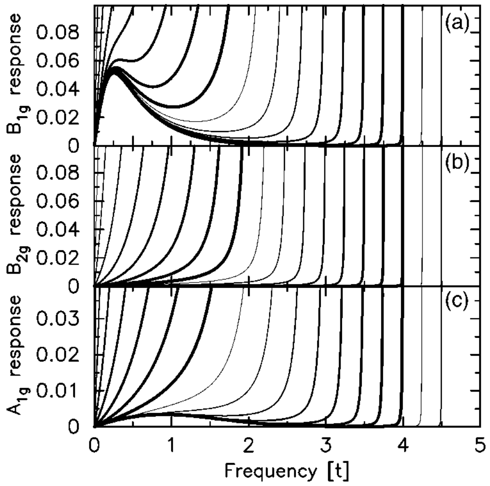

FIG. 5. Stokes Raman response for the three symmetry channels in a dirty metal with $U=0.5$. The Raman scattering response function is plotted as a function of the transfered frequency for incident photon frequencies ranging from 0.25 to 4.5 in steps of 0.25 (the thickness of the lines aids in distinguishing the different curves). This data is at low temperature ($T=0.05$) where the results are the "sharpest."

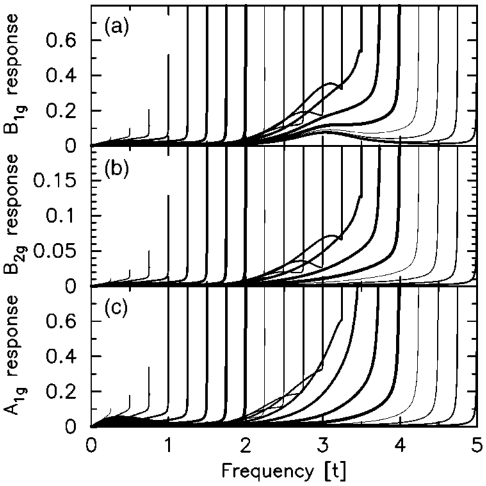

FIG. 7. Stokes Raman response for the three symmetry channels in a correlated insulator with $U=3.0$. The Raman scattering response function is plotted as a function of the transfered frequency for incident photon frequencies ranging from 0.25 to 5.0 in steps of 0.25. This data is at a high temperature ($T=1.0$) where the nonresonant response has enhanced low-energy spectral weight in B_{1g} and A_{1g} channels.

construct the imaginary parts of the Green's functions and self-energies in this regime, so all relevant quantities can be evaluated with care.[32]

We find that the Stokes response is significantly larger than the anti-Stokes response in the resonant regime, because the double resonance greatly enhances the signal when the transfered energy approaches the incident photon frequency (in the nonresonant regime, both Stokes and anti-Stokes responses are identical). Hence, we will present only the Stokes response here. We also find that, generically, the response "sharpens" as $T \rightarrow 0$, with the spectral response growing at low temperature (except for the low-energy, thermally excited response in the insulating phase).

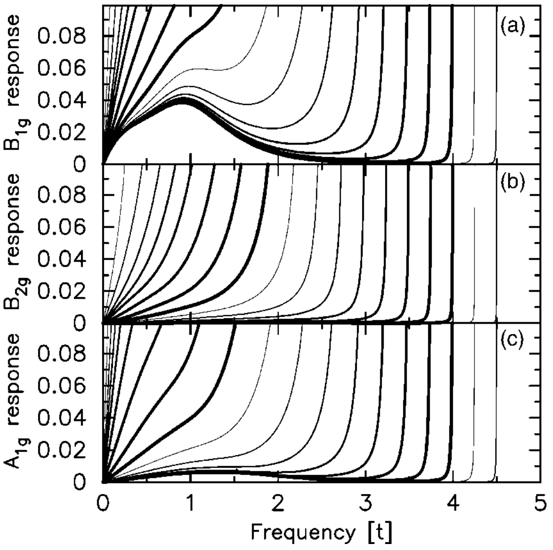

FIG. 6. Stokes Raman response for the three symmetry channels in a strongly scattering "metal" with $U=1.0$. The Raman scattering response function is plotted as a function of the transfered frequency for incident photon frequencies ranging from 0.25 to 4.5 in steps of 0.25. This data is at the temperature ($T=0.5$) where the nonresonant response has enhanced low-energy spectral weight in the B_{1g} channel.

In Figs. 5 and 6 we plot the total Raman response for $U=0.5$ and $U=1$, respectively. The former case is of a dirty metal, while the latter case is a metal that has such strong scattering that the density of states is depressed near the Fermi energy (but not so much as to create an insulator). The Stokes branch of the Raman response behaves in many respects as expected. The double resonance causes a large enhancement of the signal as the transfered frequency approaches the incident photon frequency. In the Loudon-Fleury regime, where the photon energy is much larger than the band energies, one can see a nice separation of the signal into the nonresonant and resonant (plus mixed) pieces (note that the nonresonant A_{1g} response is small due to screening effects and the nonresonant B_{2g} response vanishes due to symmetry, but the resonant effects are strong in both of these channels). In general, the resonant effects are strongest near the double resonance, and it is not true that the total response looks like the nonresonant response plus a uniform resonant enhancement, so resonant effects must be studied with care to understand the effects they play on the light scattering. Finally, note the overall similarity between panels (b) and (c) in Figs. 5 and 6. This arises from the fact that generically, the resonant effects overwhelm both nonresonant effects and mixed scattering effects, and it shows that there is not a huge variation in the resonant Raman response due to the additional renormalizations in the A_{1g} channel.

The insulating phase ($U > \sqrt{2}$) provides a number of interesting new features to the electronic Raman scattering (results for the near-critical insulator[29] at $U=1.5$ and for the small-gap insulator[20] at $U=2$ have already appeared). We begin with a discussion of a good correlated insulator $U=3$,

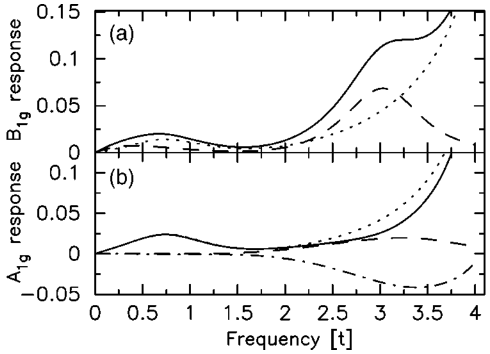

FIG. 8. Separation of different contributions to the Stokes response for $U=3$, $T=1.0$, and $\omega_i=4.0$ in the (a) B_{1g} and (b) A_{1g} channels. The solid line is the total response, the dotted line is the resonant piece, the dashed line is the nonresonant piece, and the chain-dotted line is the mixed contribution.

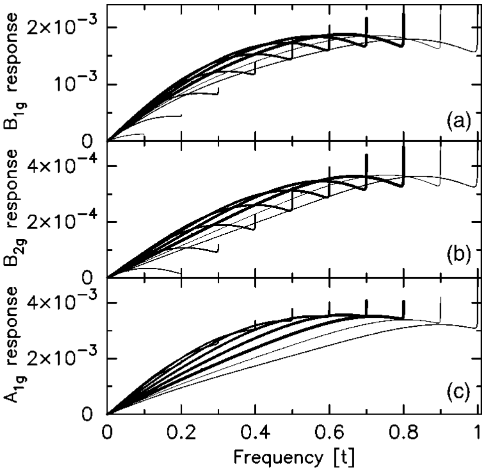

FIG. 9. Raman response at low energy for $U=3$ and $T=0.2$. The incident photon frequency changes from 0.1 to 1.0 in steps of 0.1.

which appears to have a well defined gap region in the DOS (but note that the DOS only vanishes exactly at $\omega=0$). Hence we expect there to be significant thermally driven effects in this case. To begin, we plot the Raman scattering at a fixed temperature, but with varying incident photon frequency in Fig. 7. Note that there is substantial spectral weight in both a low-energy and a high-energy peak, and that when the incident photon frequency is approximately equal to U, the high-energy (charge-transfer) peak can be enhanced significantly. But something strange occurs for higher frequencies in the A_{1g} channel. As ω_i increases beyond about 3.25, we stop to see the development of a separate charge transfer peak, and the net scattering curve looks like a simple double resonance curve even though the nonresonant response has a well-developed charge transfer peak. In other words, we are not seeing the evolution of the scattering to a simple break up of a nonresonant piece and a double resonance piece as ω_i is made large. This may not be too surprising, because in the A_{1g} channel we have nonresonant, resonant, and mixed contributions to the scattering. To illustrate how this occurs, we plot the separate contributions to the Raman scattering in Fig. 8 for the B_{1g} and $A_{1\text{g}}$ channels for $\omega_i=4.0$. In the top panel, we see the expected shape for the nonresonant curve, with both low and high energy peaks, but surprisingly, there is a strong resonant enhancement of both peaks. This is even more dramatic in the bottom panel, where the vertex corrections suppress the nonresonant low-energy peak in the A_{1g} channel, but the resonant terms bring back a strong enhancement in that region (in essence because the conservation of total charge acts to effectively screen the low-energy excitations, but the screening is much less effective for the resonant terms). The mixed contribution is small at low energy, but has a well developed charge-transfer-like feature, that is negative, and completely overwhelms, and cancels the nonresonant charge-transfer peak, leaving behind essentially a double resonance-like curve. These results are obviously quite complex. If the incident photon frequency increases further, then the peak in the mixed response moves to higher energy, and the nonresonant peak plus a higher frequency double resonance peak picture holds, but the width of the double resonance peak can be extremely narrow. One might be surprised that the double resonance peak survives in the insulator (because there are no electronic states within the gap), but in this case, we only have a pseudogap, and the states in the “gap region” are few in number, but long-lived and hence contribute to the scattering.[32]

One of the common features in resonant Raman scattering is a large enhancement of the scattering when a new scattering channel opens, as the photon frequency becomes larger than an energy gap, for example. One question to ask is does such a feature survive in a correlated system. As described above, there is no energy gap in the insulating phase (on the hypercubic lattice), but there is a region where the DOS is exponentially small, and then increases rapidly to be of order unity. One can ask whether there are features in the Raman scattering that show enhancements when the photon frequency is larger than the width of the exponentially small “gap region” of the DOS. Since the gap region for $U=3$ is about 0.5 above and below the chemical potential, we expect

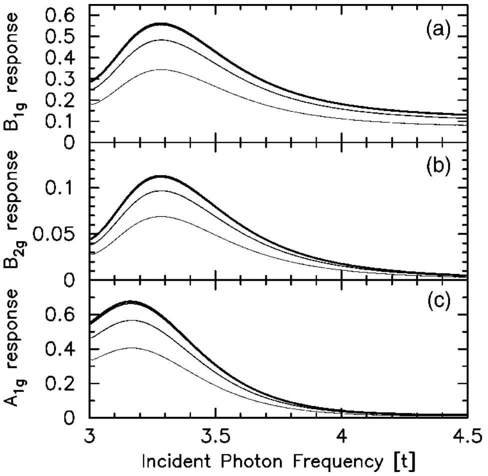

FIG. 10. Raman response at $\Omega=3$ for $U=3$ and various temperatures. The horizontal axis is the incident photon frequency. The thickest curve is $T=0.05$, and the temperature increases to 0.2, 0.5, and 1 as the curves are made thinner. Note that the curves for the lowest two temperatures are the largest, and are hard to separate.

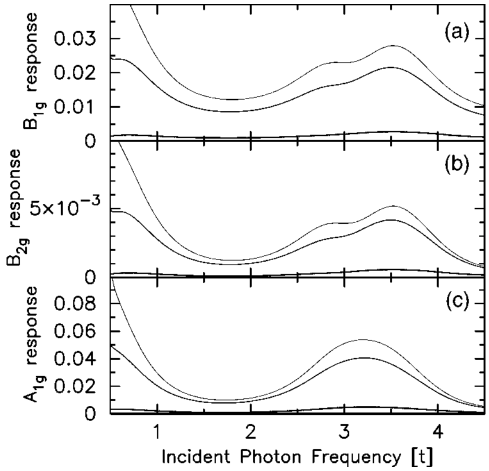

FIG. 11. Raman response at $\Omega=0.5$ for $U=3$ and various temperatures. The horizontal axis is the incident photon frequency. The thickest curve is $T=0.05$, and the temperature increases to 0.2, 0.5, and 1 as the curves are made thinner. Note that the $T=0.05$ curves are more than three orders of magnitude smaller than the $T=0.2$ curves, and cannot be distinguished from the horizontal axis in the figure.

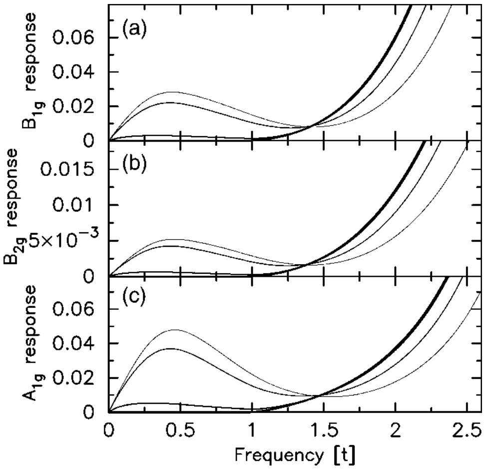

FIG. 12. Low-energy isosbestic behavior of the resonant Raman response for $U=3$ and $\omega_i=3.5$. The different thicknesses correspond to different temperatures, with thicker curves corresponding to lower temperatures (four curves are plotted for $T=1$, 0.5, 0.2, and 0.05). Note how the curves all cross at an isosbestic point, just slightly smaller than $U/2$.

interesting results for photon frequencies near 0.5. We plot the Raman scattering for ω_i increasing from 0.1 to 1 in steps of 0.1 in Fig. 9 for low temperature ($T=0.2$). Note how small the overall scale of the Raman scattering is. We see different behavior in the B_{1g} and B_{2g} sectors versus the A_{1g} sector. In panels (a) and (b) we see the low energy scattering increases as ω_i increases until ω_i reaches approximately 0.5, where it starts to decrease. The increasing behavior is essentially this resonant enhancement due to the opening of scattering channels as the photon frequency becomes larger than the gap. Note how this phenomenon essentially does not occur in panel (c), where the curves lie below each other as ω_i is increased. Hence the A_{1g} channel does not show the analogue of this resonant-enhancement effect. The effect disappears in all channels once the temperature becomes larger than about 0.5, where thermal excitations can be easily made across the "gap region." Note, furthermore, that the largest resonant effects occur not when the scattering channel first opens, but rather when $\omega_i\approx U$ because that is the value of frequency that separates the peaks in the single-particle DOS, and hence it corresponds to the strongest scattering from occupied to unoccupied states.

We saw in Fig. 8 that there is a resonant enhancement at low energy when the incident photon frequency is close to U in size. To examine this phenomenon further, we plot the total Raman scattering at a fixed transfered photon frequency (chosen to be 0.5 for the low-energy peak and 3.0 for the high-energy peak) as a function of the incident photon frequency in Figs. 10 and 11.

In Fig. 10, we see expected behavior. The charge-transfer peak at $\Omega=U=3$ has a resonant enhancement for photon frequencies slightly higher than U, then a suppression to the nonresonant peak values at the highest incident frequencies (except for the A_{1g} channel, where the charge transfer peak is initially suppressed until the incident photon frequency is larger than about 6, due to the cancellation from the mixed diagrams described above). The width of the resonant peak is about 0.5, and it is pushed to higher frequency in the B_{1g} and B_{2g} channels. In Fig. 11, we find an interesting joint resonance effect. There is a resonant enhancement near $\omega_i=0.5$, that comes from the double resonance. In addition, there is another broad resonance effect centered just slightly higher than $\omega_i=U=3$, where both the charge-transfer and the low-energy peaks resonate at the same incident photon frequency. In the A_{1g} channel, the joint resonance peak is a single smooth peak, while in the B_{1g} and B_{2g} channels, the joint resonance peak seems to have a double-peak structure to it. As the temperature is reduced, the resonant effects remain, but the spectral weight in the low-energy peak gets suppressed to very small values (the $T=0.05$ curves are indistinguishable from the horizontal axis because they are at least three orders of magnitude smaller than the $T=0.2$ curves). The evolution of the resonant profile for other values of transferred frequency Ω is complex and can be found in Ref. 28 for $U=3$.

The low-energy isosbestic behavior (which means that the Raman response is independent of temperature at a characteristic frequency) is plotted in Fig. 12. We choose $\omega_i=3.5$ because it corresponds to the maximal joint resonance effect for both the charge-transfer and low-energy peaks. We find that the low-energy isosbestic behavior is generic for the resonant Raman scattering, with the response curves crossing at $\Omega\approx U/2=1.5$ for all symmetries. Hence, the low-energy isosbestic behavior seen in the nonresonant response (which was most apparent in the B_{1g} channel, but can also be seen in the A_{1g} channel when the response is plotted on a logarithmic scale[28]), survives in the resonant cases as well, and this helps explain why it is seen in so many experimental systems. In addition to the low-energy isosbestic point shown in Fig. 12 at $\Omega\approx U/2$, there is a second isosbestic point[28] that appears near the double resonance $\Omega\approx\omega_i$. Starting from large ω_i ($\Omega_i>U$), as ω_i is reduced, the two isosbestic points move closer to each other, eventually joining together and disappearing when $\omega_i \approx U/2$. So the isosbestic behavior will not be seen if the incident photon frequency is too low.

V. DISCUSSION

With the use of DMFT, we solved for the full Raman response for all frequencies of incoming light in the Falicov-Kimball model. Since the Falicov-Kimball model can be tuned across a metal-insulator transition, we have determined the form of Raman scattering in both the metallic and insulating states, and have investigated light scattering on both sides of the quantum critical point at $U=\sqrt{2}$. Resonant, nonresonant, and mixed contributions have all been treated on an equal footing and we allowed for an analysis of the dependence of Raman scattering with temperature, interactions, and different light polarizations.

Our results confirm a number of previously held beliefs. First, we find a strong resonant enhancement of the charge-transfer peak in Raman scattering when the incident photon energy lies near the charge-transfer energy. This behavior is robust to temperature and polarization changes due to the local nature of the charge-transfer excitation in our model. Second, we also find a polarization-independent “double-resonance” enhancement when the transfered frequency of the light approaches the incident light frequency. This feature survives in the insulating phase because of the pseudogap nature of the insulator on the hypercubic lattice.

In addition, we find a number of new features of light scattering in correlated insulators. We find that low energy spectral features, related to thermal populations of elementary excitations, show resonance behavior when the incident light is tuned to the much higher frequency of the charge-transfer energy. This is a specific case where the correlations are crucial, since in uncorrelated materials, this would correspond to off-resonant conditions. Yet due to the many-body nature of the correlated band, spectral features well separated from the charge transfer peak have a non-trivial resonance profile. We believe that these may be potentially useful to understand the complex nature of charge excitations in correlated materials as it would impact both electronic and phononic Raman scattering at low frequencies. Finally, we find that the presence of an isosbestic point in the Raman response for correlated insulators results from a symmetry-dependent combination of all resonant, mixed, and nonresonant terms, and appears to be generic.

We close with a discussion of open questions concerning improvements to the theory. Here we have restricted ourselves to Raman scattering in a correlated band of electrons in the limit of large spatial dimensions. Performing calculations in physical dimensions requires more many-particle charge vertex renormalizations which makes the problem extremely difficult, though possible in principle. But we found that most vertex renormalizations were rather mild, so including nonlocal effects into the vertices (finite dimensions) probably does not change these results dramatically (unless the vertex can diverge in finite dimensions). In addition, $\boldsymbol{q}$-dependent information would prove to be useful for investigating dispersive many-particle excitations, as probed in inelastic x-ray scattering. These are topics of future interest.

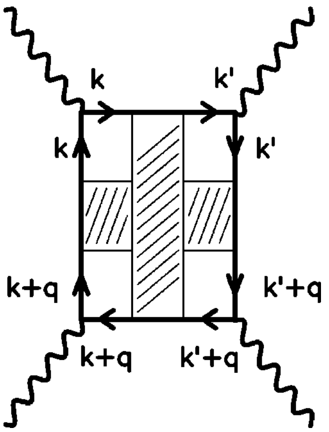

FIG. 13. Feynman diagrams for a typical parquetlike renormalization. This resonant diagram has a simultaneous horizontal and vertical renormalization by the two-particle reducible charge vertex. Note that such a renormalization is only possible in the A_{1g} sector.

ACKNOWLEDGMENTS

The research described in this publication was made possible in part by Grant No. UP2-2436-LV-02 of the U.S. Civilian Research and Development Foundation (CRDF). A.M.S. and O.V. acknowledge support from the Fundamental Researches State Fund of the Ministry for Education and Science of Ukraine under Grant No 02.07/266. J.K.F. also acknowledges support from the National Science Foundation under Grant No. DMR-0210717. T.P.D. would like to acknowledge NSERC, PREA and the Alexander von Humboldt Foundation for support of this work.

APPENDIX A: PARQUET CONTRIBUTIONS

In addition to the diagrams presented in Fig. 3, there can also be parquet-like contributions with both vertical and horizontal renormalizations. One type of these diagrams is shown in Fig. 13. The corresponding expression has the form

$$\frac{t^{*4}}{D^2}\frac{1}{N^3}\sum_{\substack{\boldsymbol{q}\boldsymbol{k}\boldsymbol{k}'\\ \alpha\beta\alpha'\beta'}} \sin k_\alpha \sin(k_\beta + q_\beta)\sin k'_{\alpha'} \sin(k'_{\beta'} + q_{\beta'}) \\ \times T^2\Gamma(1,3)\Gamma(2,4)G_1(\boldsymbol{k}')G_2(\boldsymbol{k}')G_2(\boldsymbol{k}'+\boldsymbol{q})G_3(\boldsymbol{k}'+\boldsymbol{q}) \\ \times G_2(\boldsymbol{k}+\boldsymbol{q})G_4(\boldsymbol{k}+\boldsymbol{q})G_4(\boldsymbol{k})G_1(\boldsymbol{k}). \tag{A1}$$

In the expression in Eq. (A1), all the momentum dependence (in the $D=\infty$ limit) is contained in the band energy [see Eq. (3.3)] and, after expanding the products of the Green’s functions with the same momentum into partial fractions over $\epsilon_{\boldsymbol{k}}$, the summations over momentum are of the form

$$\frac{t^{*4}}{D^2}\frac{1}{N}\sum_{\boldsymbol{q}}\left[\frac{1}{N}\sum_{\boldsymbol{k}}\sum_{\alpha\beta}\frac{\sin k_\alpha \sin(k_\beta+q_\beta)}{(Z_1-\epsilon_{\boldsymbol{k}})(Z_2-\epsilon_{\boldsymbol{k}+\boldsymbol{q}})}\right] \\ \times\left[\frac{1}{N}\sum_{\boldsymbol{k}'}\sum_{\alpha'\beta'}\frac{\sin k'_{\alpha'} \sin(k'_{\beta'}+q_{\beta'})}{(Z_3-\epsilon_{\boldsymbol{k}'})(Z_4-\epsilon_{\boldsymbol{k}'+\boldsymbol{q}})}\right]. \tag{A2}$$

In the same way as was done for Eq. (3.16), we find the expression in the bracket reduces to the following in the $D \to \infty$ limit $[\zeta_i = \mathrm{sgn}(\mathrm{Im}\, Z_i)]$

$$i^2 \int_0^{\zeta_1 \infty} d\lambda_1 \int_0^{\zeta_2 \infty} d\lambda_2 e^{-i(\lambda_1 Z_1 + \lambda_2 Z_2)} e^{-t^2(\lambda_1^2 + \lambda_2^2 + 2\lambda_1 \lambda_2 X_q)/4} \times \left[\frac{1}{2} \sum_{\alpha} \cos q_\alpha + \frac{t^{*2} \lambda_1 \lambda_2}{4D} \sum_{\alpha \neq \beta} \sin q_\alpha \sin q_\beta \right], \tag{A3}$$

where $X_{\boldsymbol{q}} = \lim_{D\to\infty}(1/D)\Sigma_{\alpha=1}^{D} \cos q_\alpha$. The main contribution comes from the first term in Eq. (A3) and there is a similar term in the second bracket of Eq. (A2). Replacing the square of a cosine by its average value $\frac{1}{2}$, we find that Eq. (A2) reduces to

$$\lim_{D\to\infty} \frac{t^{*4}}{8D} G_1 G_2 G_3 G_4 \to 0 \tag{A4}$$

which vanishes as $D \to \infty$. A similar procedure can be performed for all other terms with a parquet-like renormalization. Hence, the parquet-like contributions are unimportant for resonant Raman scattering in large dimensions.

---

*Electronic address: ashv@icmp.lviv.ua; URL: http://ph.icmp.lviv.ua/~ashv/

†Electronic address: vorobyov@icmp.lviv.ua; URL: http://ph.icmp.lviv.ua/~vorobyov/

‡Electronic address: freericks@physics.georgetown.edu; URL: http://www.physics.georgetown.edu/~jkf/

§Electronic address: tpd@lorax.uwaterloo.ca; URL: http://www.sciborg.uwaterloo.ca/~tpd/

[1] P. Nyhus, S. L. Cooper, and Z. Fisk, Phys. Rev. B **51**, R15 626 (1995).

[2] P. Nyhus, S. L. Cooper, Z. Fisk, and J. Sarrao, Phys. Rev. B **52**, R14 308 (1995); **55**, 12 488 (1997).

[3] H. L. Liu, S. Yoon, S. L. Cooper, G. Cao, and J. E. Crow, Phys. Rev. B **60**, R6980 (1999).

[4] K. B. Lyons, P. A. Fleury, L. F. Schneemeyer, and J. V. Waszczak, Phys. Rev. Lett. **60**, 732 (1988); S. Sugai, S. I. Shamoto, and M. Sato, Phys. Rev. B **38**, 6436 (1988); P. E. Sulewski, P. A. Fleury, K. B. Lyons, S.-W. Cheong, and Z. Fisk, *ibid.* **41**, 225 (1990); R. Liu, M. V. Klein, D. Salamon, S. L. Cooper, W. C. Lee, S.-W. Cheong, and D. M. Ginsberg, J. Phys. Chem. Solids **54**, 1347 (1993).

[5] G. Blumberg, P. Abbamonte, M. V. Klein, W. C. Lee, D. M. Ginsberg, L. L. Miller, and A. Zibold, Phys. Rev. B **53**, R11 930 (1996).

[6] J. G. Naeini, X. K. Chen, J. C. Irwin, M. Okuya, T. Kimura, and K. Kishio, Phys. Rev. B **59**, 9642 (1999).

[7] J. K. Freericks and T. P. Devereaux, Condens. Matter Phys. **4**, 149 (2001); J. K. Freericks and T. P. Devereaux, Phys. Rev. B **64**, 125110 (2001).

[8] J. K. Freericks, T. P. Devereaux, and R. Bulla, Acta Phys. Pol. B **32**, 3219 (2001); Phys. Rev. B **64**, 233114 (2001); Acta Phys. Pol. B **34**, 737 (2003); J. K. Freericks, T. P. Devereaux, R. Bulla, and Th. Pruschke, Phys. Rev. B **67**, 155102 (2003).

[9] T. P. Devereaux, G. E. D. McCormack, and J. K. Freericks, Phys. Rev. Lett. **90**, 067402 (2003); Phys. Rev. B **68**, 075105 (2003).

[10] A. V. Chubukov and D. M. Frenkel, Phys. Rev. B **52**, 9760 (1995); Phys. Rev. Lett. **74**, 3057 (1995); D. K. Morr and A. V. Chubukov, Phys. Rev. B **56**, 9134 (1997).

[11] T. Tohyama, H. Onodera, K. Tsutsui, and S. Maekawa, Phys. Rev. Lett. **89**, 257405 (2002).

[12] P. A. Fleury and R. Loudon, Phys. Rev. **166**, 514 (1968).

[13] R. R. P. Singh, Comments Condens. Matter Phys. **15**, 241 (1991).

[14] E. Dagotto and D. Poilblanc, Phys. Rev. B **42**, 7940 (1990); E. Gagliano and S. Bacci, *ibid.* **42**, R8772 (1990).

[15] A. W. Sandvik, S. Capponi, D. Poilblanc, and E. Dagotto, Phys. Rev. B **57**, 8478 (1998).

[16] D. K. Morr, A. V. Chubukov, A. P. Kampf, and G. Blumberg, Phys. Rev. B **54**, 3468 (1996).

[17] R. R. P. Singh, P. A. Fleury, K. B. Lyons, and P. E. Sulewski, Phys. Rev. Lett. **62**, 2736 (1989).

[18] C. M. Canali and S. M. Girvin, Phys. Rev. B **45**, 7127 (1992).

[19] A. A. Katanin and A. P. Kampf, Phys. Rev. B **67**, 100404(R) (2003).

[20] A. M. Shvaika, O. Vorobyov, J. K. Freericks, and T. P. Devereaux, Phys. Rev. Lett. **93**, 137402 (2004).

[21] V. Janis, Phys. Rev. Lett. **83**, 2781 (1999).

[22] A. Georges, G. Kotliar, W. Krauth, and M. J. Rozenberg, Rev. Mod. Phys. **68**, 13 (1996).

[23] V. Janis, Phys. Rev. B **64**, 115115 (2001).

[24] L. M. Falicov and J. C. Kimball, Phys. Rev. Lett. **22**, 997 (1969).

[25] B. S. Shastry and B. I. Shraiman, Phys. Rev. Lett. **65**, 1068 (1990); Int. J. Mod. Phys. B **5**, 365 (1991).

[26] U. Brandt and C. Mielsch, Z. Phys. B: Condens. Matter **75**, 365 (1989); **79**, 295 (1990).

[27] A. M. Shvaika, Physica C **341–348**, 177 (2000); J. K. Freericks and P. Miller, Phys. Rev. B **62**, 10022 (2000); A. M. Shvaika, J. Phys. Stud. **5**, 349 (2001).

[28] A. Shvaika, O. Vorobyov, J. K. Freericks, and T. P. Devereaux, cond-mat/0407120.

[29] A. Shvaika, O. Vorobyov, J. K. Freericks, and T. P. Devereaux, cond-mat/0406305, Physica B (to be published).

[30] R. M. Martin and L. M. Falicov, in *Light Scattering in Solids*, edited by M. Cardona (Springer-Verlag, New York, 1975).

[31] D. O. Demchenko, A. V. Joura, and J. K. Freericks, Phys. Rev. Lett. **92**, 216401 (2004).

[32] J. K. Freericks, D. O. Demchenko, A. V. Joura, and V. Zlatić, Phys. Rev. B **68**, 195120 (2003).